

1 Simulating carbon and water fluxes using a coupled process-based  
2 terrestrial biosphere model and joint assimilation of leaf area index  
3 and surface soil moisture

4 **Sinan Li**<sup>1,2</sup>, **Li Zhang**<sup>1,3,\*</sup>, **Jingfeng Xiao**<sup>4</sup>, **Rui Ma**<sup>5</sup>, **Xiangjun Tian**<sup>6</sup>, **Min Yan**<sup>1,3</sup>

5 <sup>1</sup> Key Laboratory of Digital Earth Science, Aerospace Information Research Institute, Chinese Academy of Sciences, No. 9  
6 Dengzhuang South Road, Beijing 100094, China.

7 <sup>2</sup> College of Resources and Environment, University of Chinese Academy of Sciences, No. 19A Yuquan Road, Beijing 100049, China

8 <sup>3</sup> Key Laboratory of Earth Observation of Hainan Province, Sanya 572029, China

9 <sup>4</sup> Earth Systems Research Center, Institute for the Study of Earth, Oceans, and Space, University of New Hampshire, Durham, New  
10 Hampshire 03824, USA

11 <sup>5</sup> School of Remote Sensing and Information Engineering, Wuhan University, Wuhan 430079, China

12 <sup>6</sup> International Center for Climate and Environment Sciences (ICCES), Institute of Atmospheric Physics, Chinese Academy of Sciences,  
13 Beijing 100029, China

14  
15 \* Correspondence: zhangli@aircas.ac.cn; Tel.: +86-10-8217-8193

19 **Abstract:**

20       Reliable modeling of carbon and water fluxes is essential for understanding the terrestrial carbon  
21 and water cycles and informing policy strategies aimed at constraining carbon emissions and improving  
22 water use efficiency. We designed an assimilation framework (LPJ-Vegetation and soil moisture Joint  
23 Assimilation, or LPJ-VSJA) to improve gross primary production (GPP) and evapotranspiration (ET)  
24 estimates globally. The integrated model, LPJ-PM as the underlying model, coupled from the Lund-  
25 Potsdam-Jena Dynamic Global Vegetation Model (LPJ-DGVM version 3.01) and a hydrology module  
26 (i.e., the updated Priestley–Taylor Jet Propulsion Laboratory model, PT-JPL<sub>SM</sub>). Satellite-based soil  
27 moisture products derived from the Soil Moisture and Ocean Salinity (SMOS) and Soil Moisture Active  
28 and Passive (SMAP) and leaf area index (LAI) from the global Land and Ground satellite (GLASS)  
29 product were assimilated into LPJ-PM to improve GPP and ET simulations using a Proper Orthogonal  
30 Decomposition-based ensemble four-dimensional variational assimilation method (POD<sub>En4DVar</sub>). The  
31 joint assimilation framework LPJ-VSJA achieved the best model performance (with an  $R^2$  of 0.91 and  
32 0.81 and an ubRMSD reduced by 40.3% and 29.9% for GPP and ET, respectively, compared with those  
33 of LPJ-DGVM at the monthly scale). The assimilated GPP and ET demonstrated a better performance in  
34 the arid and semi-arid regions (GPP:  $R^2=0.73$ , ubRMSD=1.05 g C m<sup>-2</sup> d<sup>-1</sup>; ET:  $R^2=0.73$ , ubRMSD= 0.61  
35 mm d<sup>-1</sup>) than in the humid and sub-dry humid regions (GPP:  $R^2=0.61$ , ubRMSD=1.23 g C m<sup>-2</sup> d<sup>-1</sup>; ET:  
36  $R^2=0.66$ ; ubRMSD=0.67 mm d<sup>-1</sup>). The ET simulated by LPJ-PM that assimilated SMAP or SMOS had a  
37 slight difference, and the SMAP soil moisture data performed better than that SMOS data. Our global  
38 simulation modeled by LPJ-VSJA was compared with several global GPP and ET products (e.g., GLASS

39 GPP, GOSIF GPP, GLDAS ET, GLEAM ET) using the triple collocation (TC) method. Our products,  
40 especially ET, exhibited advantages in the overall error distribution (estimated error ( $\mu$ ): 3.4 mm month<sup>-1</sup>;  
41 estimated standard deviation of  $\mu$ : 1.91 mm month<sup>-1</sup>). Our research showed that the assimilation of  
42 multiple datasets could reduce model uncertainties, while the model performance differed across regions  
43 and plant functional types. Our assimilation framework (LPJ-VSJA) can improve the model simulation  
44 performance of daily GPP and ET globally, especially in water-limited regions.

45 **Keywords:** Data Assimilation; SMOS; SMAP; Gross primary production (GPP); evapotranspiration  
46 (ET); GLASS LAI

47

---

## 48 **1. Introduction**

49 Gross primary production (GPP) and evapotranspiration (ET) are essential components of the carbon  
50 and water cycles. Carbon and water fluxes are inherently coupled on multiple spatial and temporal scales  
51 (Law et al. 2002; Sun et al. 2019; Waring and Running 2010). Terrestrial biosphere models are the most  
52 sophisticated approach for providing a relatively detailed description of such interdependent relationships  
53 regarding water and carbon fluxes and understanding the response of terrestrial ecosystems to changes in  
54 atmospheric CO<sub>2</sub> and climate (Kaminski et al. 2017). The dynamic global vegetable models (DGVMs)  
55 are process-based dynamic terrestrial biosphere models, which can simulate material exchange between  
56 vegetation and different conditions from the perspective of vegetation physiological processes, and are  
57 widely used to estimate carbon and water fluxes of terrestrial vegetation. However, there are still large

58 uncertainties in carbon and water flux estimates at regional to global scales. Both diagnostic and  
59 prognostic models show substantial differences in the magnitude and spatiotemporal patterns of GPP and  
60 ET. For example, the global annual GPP estimates exhibited a large range (130–169 Pg C yr<sup>-1</sup>) among 16  
61 process-based terrestrial biosphere models (Anav et al. 2015). The global ET ranged from 70,000 to  
62 75,000 km<sup>3</sup> yr<sup>-1</sup>, and the uncertainty of regional or global ET estimates was up to 50% of the annual mean  
63 ET value, especially in the semi-arid regions (Miralles et al. 2016). These uncertainties mainly arise from  
64 the forcing datasets, simplification of mechanisms or imperfect assumptions in processes, and uncertain  
65 parameters in the processed models and assimilation methods (Xiao et al. 2019).

66 In the last two decades, remote sensing products have been assimilated into DGVM<sub>S</sub> to reduce the  
67 uncertainty in modeled carbon and water fluxes (MacBean et al. 2016; Scholze et al. (2017); Exbrayat  
68 et al. (2019)). Data assimilation (DA) is an effective approach to reduce uncertainties in terrestrial  
69 biosphere models by integrating satellite products with models to constrain related parameters or state  
70 variables. A DA system contains four main components: a set of observations, an observation operator,  
71 an underlying model, and an assimilation method. The assimilation method considers the errors from both  
72 models and observations, and reduces model uncertainties by minimizing a cost function. The Ensemble  
73 Kalman Filter (EnKF) has been widely applied in land surface process models for parameter optimization,  
74 which significantly improve simulations by periodically updating state variables (e.g., LAI and soil  
75 moisture) using remote sensing data without altering the model structure (Ines et al. 2013; Li et al. 2017;  
76 Ma et al. 2013). Yet, the EnKF relies on the instantaneous observations to update the state variable at the  
77 current time, and gives the predicted value at the next time based on the forward integration of the updated

78 state variable. The four-dimensional variational method (4DVar) assimilation method can obtain the  
79 dynamic balance of the estimation in the time window when it is applied to the long-series forecast model  
80 (Barth et al. 2014; Zhang et al. 2014). In particular, the Proper Orthogonal Decomposition (POD)-based  
81 ensemble 4DVAR assimilation method (referred to as PODEn4DVar) (Tian and Feng 2015) requires  
82 relatively less computation and can simultaneously assimilate the observations at different time intervals.  
83 Meanwhile, it maintains the structural information of the four-dimensional space. This method has a  
84 satisfactory performance in land DA for carbon and water variables (Tian et al. 2009; Tian et al. 2010)  
85 and can better estimate GPP and ET than EnKF (Ma et al. 2017).

86 Multiple sources of remote sensing data streams have been used to constrain models for assimilation.  
87 As a critical biophysical parameter of the land, leaf area index (LAI) is closely related to many land  
88 processes, such as photosynthesis, respiration, precipitation interception, ET, and surface energy  
89 exchange (Fang et al. 2019). LAI is highly sensitive to the simulation of carbon and water fluxes (Liu et  
90 al. 2018), and accurate LAI estimates can improve the simulations of the carbon and water fluxes (Bonan  
91 et al. 2014;; Mu et al. 2007). Soil moisture is a major driving factor affecting vegetation production in  
92 arid ecosystems, especially, in semi-arid areas (Liu et al. 2020). Introducing surface soil moisture (SSM)  
93 into the model can significantly improve GPP and ET simulation, particularly in water-limited areas (He  
94 et al. 2017; Li et al. 2020).

95 The advancement of earth observation, machine learning, inversion algorithms, and computer  
96 technology has improved the accuracy of global LAI products and boosted model-data fusion studies  
97 (Fang et al. 2019; Kganyago et al. 2020; Xiao et al. 2017). The Advanced Very High-Resolution

98 Radiometer (AVHRR) generates global LAI products with the longest historic record (since the early  
99 1980s). The GLASS LAI product has been verified to have a better accuracy than that of MODIS and  
100 CYCLOPES and is more temporally continuous and spatially complete (Xiao et al. 2013). Several recent  
101 studies showed that the assimilation of GLASS LAI into DGVMs enhanced the performance of the  
102 models in simulating carbon cycling (e.g., GPP, Net Ecosystem Exchange (NEE)) and hydrological (e.g.,  
103 ET, SM) processes (Ling et al. 2019; Ma et al. 2017; Yan et al. 2016).

104        Microwave remote sensors are considered effective tools for measuring SM globally (Petropoulos et  
105 al. 2015). For example, surface SM products have been derived from the Soil Moisture and Ocean Salinity  
106 (SMOS) and Soil Moisture Active and Passive (SMAP) satellites equipped with an L-band microwave  
107 instrument. The products from these satellites have been evaluated against in-situ observations and other  
108 SM products and overall have high accuracy (Burgin et al. 2017; Cui et al. 2018). Additionally, the SMAP  
109 performs better than SMOS and other SM products (e.g., Advanced Scatterometer (ASCAT), Advanced  
110 Microwave Scanning Radiometer 2 (AMSR2)) with an overall lower error and a higher correlation based  
111 on the verification with in-situ SM data from 231 sites (Cui et al. 2018; Kim et al. 2018). The assimilation  
112 of SMAP data can improve the simulation accuracy of carbon and water fluxes (He et al. 2017; Li et al.  
113 2020) and hydrological variables (surface soil moisture, root-zone soil moisture, and streamflow)  
114 (Blyverket et al. 2019; Koster et al. 2018; Reichle et al. 2017). In addition, the assimilation of SMAP data  
115 performed slightly better than that of SMOS and ESA CCI data (Blyverket et al. 2019).

116        In the nonlinear model or nonlinear observation operator, only simultaneous assimilation makes  
117 optimal use of observations (MacBean et al. 2016). Therefore, a joint assimilation of soil moisture and

118 LAI can make full use of the two variables. From site (Albergel et al. (2010);Rüdiger et al. (2010); Wu et  
119 al.,2018) to regional assimilation (Ines et al. (2013)), many studies have proposed that joint assimilation  
120 of vegetation parameters and soil moisture is a potential improvement in modeling the carbon-water cycle.  
121 For instance,. joint assimilation of soil moisture and leaf area index can improve the accuracy of crop  
122 yield estimation (Xie et al.,2018; Pan et al.,2019), with small region and high spatial resolution, which  
123 adopting observation data from stations or high-resolution satellites (e.g. Sentinel-1 and 2). At a large  
124 regional scale, Bonan et al. (2020) assimilated LAI and SM together into the Interactions between Soil,  
125 Biosphere and Atmosphere (ISBA) land model and improved the modeled GPP, ET, and runoff in the  
126 Mediterranean region. Rahman et al. (2022) jointly assimilates GLASS LAI and SMAP soil moisture to  
127 improve water and carbon flux simulations within the Noah-MP model over the CONUS domain.  
128 Albergel et al.(2020) jointly assimilates the ASCAT soil moisture index (SMI) and LAI GEOV1 into  
129 ISBA (Interaction between Soil Biosphere and Atmosphere) surface model through the Global Offline  
130 Land Data assimilation system LDAS-Model to monitor extreme events such as drought and Heatwave  
131 events. In conclusion, Kalman Filter and its variant methods are mostly used joint assimilation methods  
132 at regional scale, which requires many kinds of observation data and their accuracy directly affects the  
133 assimilation performance.

134 This study stems from the researches discussed above and further explored the potential of joint  
135 assimilating satellite LAI and soil moisture products globally. Specifically, it was the first time that an  
136 updated LPJ-DGVM model was used to jointly assimilate GLASS LAI and SMAP soil moisture for  
137 simulating global water and carbon fluxes. The latest global soil moisture datasets (SMOS and SMAP)

138 were used, and the assimilation performance of these two observations was analyzed. Since previous work  
 139 showed the importance of surface soil moisture in the semi-arid and arid areas, one of the specific  
 140 objectives of our study is to compare the assimilation effect in the humid and arid areas and improve the  
 141 understanding of the effect of surface soil moisture on vegetation activity in wet and dry zones. In addition,  
 142 compared with the assimilation methods in previous studies (mostly using Kalman Filter variants), the  
 143 POD-En4DVar method is used, which greatly improves the computational efficiency.

## 144 **2. LPJ-VSJA framework and assimilation strategy**

### 145 *2.1. Coupled- model (LPJ-PM) for assimilation*

146 In this study, a coupled terrestrial biosphere model, LPJ-PM, was used to simulate daily GPP and  
 147 ET by assimilating satellite-derived LAI and SM. The LPJ-PM is coupled from LPJ-DGVM and PT-  
 148 JPL<sub>SM</sub>. The original input data in PT-JPL<sub>SM</sub> were all inherited from LPJ-DGVM, with the exception of  
 149 relative humidity (RH) and surface soil moisture (SMOS and SMAP), including the initial LAI calculated  
 150 by the LPJ-DGVM or assimilated LAI obtained through the LAI assimilation scheme, canopy height, and  
 151 the fraction of absorbed photosynthetic effective radiation (fAPAR). The detailed processes of the LPJ-  
 152 PM have been described in Li et al. (2020), and the flow chart for the coupling is shown in Figure 1.

153 **Table 1. Description of the models and outputs in this study**

acronyms	Full name	Description	Output
LPJ-DGVM	Lund-Potsdam-Jena	This model is used as a model	GPP <sub>LPJ</sub> , ET <sub>LPJ</sub>



---

(Sitch et al. 2003)	Dynamic Global Vegetation Model	operator to simulated initial ET	
PT-JPL <sub>SM</sub>	Updated Priestley–Taylor Jet Propulsion Laboratory model	The model is used as a module of the LPJ-PM and establishes a connection between SMAP SM and ET	N/A
(Purdy et al. (2018))			
LPJ-PM (Li et al. (2020))	Lund-Potsdam-Jena and Updated Priestley–Taylor Jet Propulsion Laboratory coupled model	An integrated model coupled from the PT-JPL <sub>SM</sub> and LPJ-DGVM	GPP <sub>SM</sub> , ET <sub>PM</sub>
LPJ-VSJA (this study)	Lund-Potsdam-Jena Vegetation-Soil moisture-Joint - Assimilation system	A process-based assimilation framework for assimilating LAI and SSM jointly into LPJ-PM	GPP <sub>LAI</sub> , ET <sub>LAI</sub> ; GPP <sub>SM</sub> , ET <sub>SM</sub> ; GPP <sub>CO</sub> ; ET <sub>CO</sub>

---

154

### 155 2.1.1 LPJ-DGVM

156 The LPJ-DGVM is a process-oriented dynamic model, which considers mutual interaction of carbon  
 157 and water cycling and is designed to simulate vegetation distribution and carbon, soil and atmosphere  
 158 fluxes (Sitch et al. 2003). For each plant functional type (PFT), the GPP is calculated by implementing  
 159 coupled photosynthesis and water balance

160 The canopy GPP is updated daily:

$$161 \quad GPP = \frac{(J_E + J_C - \sqrt{(J_E + J_C)^2 - 4\theta J_E J_C})}{2\theta} \quad (2.1)$$

162 where  $J_C$  is the Rubisco limiting rate of photosynthesis,  $J_E$  is the light limiting rate of photosynthesis, and  
163 the empirical parameter  $\theta$  represents the common limiting effect between the two terms.  $J_E$  is related to  
164 APAR (absorbed photosynthetic radiation, product of FPAR and PAR), while  $J_C$  is related to  $V_{Cmax}$   
165 (canopy maximum carboxylation capacity,  $\mu \text{ mol CO}_2/\text{m}^2/\text{s}$ ):

$$166 \quad J_E = C_1 \text{APAR} \quad (2.2)$$

$$167 \quad J_C = C_2 V_{C \max} \quad (2.3)$$

168 where  $C_1$  and  $C_2$  are determined by a variety of photosynthetic parameters and the intercellular partial  
169 pressure of  $\text{CO}_2$ , which is related to atmospheric  $\text{CO}_2$  content and further altered by leaf stomatal  
170 conductance (Sitch et al. 2003). APAR and FPAR are directly related to LAI.

171 In the water cycle module, ET is calculated as the minimum of a plant- and soil-limited supply  
172 function ( $E_{\text{supply}}$ ) and the atmospheric demand ( $E_{\text{demand}}$ ) (Haxeltine and Prentice 1996; Sitch et al.  
173 2003). The soil structure is simplified to a “two-layer bucket” model (the top soil layer at a 0-50 cm depth  
174 and the bottom layer at a 50-100 cm depth) .

$$175 \quad E_S = E_p \times W_{r_{20}} \times (1 - fv) \quad (2.4)$$

176 In this module, it is assumed that the soil layer above 20 cm produces water through evaporation,  
 177 and  $Wr_{20}$  is the relative water content of the soil above 20 cm, which is used as the only soil water limit  
 178 for calculating vegetation transpiration and soil evaporation. In the evapotranspiration estimation, the  
 179 over-simplification of soil structure and soil water limitation lead to a large error (Sitch et al. 2003), while  
 180 LPJ-DGVM cannot directly assimilate surface soil water due to the limitation of soil layer stratification  
 181 , and therefore, the satellite-derived surface SM cannot be assimilated into LPJ-DGVM directly. The  
 182 oversimplified soil structure and single soil moisture limitation inevitably lead to sizeable uncertainty in  
 183 ET simulation. Additionally, the monthly input caused a daily variation of the modeled SM, which was  
 184 also not transmitted to the calculation of GPP and ET. Thus, the updated PT-JPL model (hereafter referred  
 185 to as PT-JPL<sub>SM</sub>) was coupled with LPJ-DGVM and the model structure was modified so that surface SM  
 186 can be directly assimilated into the coupled model at the daily time step.

### 187 2.1.2 PT-JPL<sub>SM</sub>

188 In PT-JPL<sub>SM</sub>, three ET components are modelled: soil evaporation (E), vegetation transpiration (T),  
 189 and leaf evaporation (I). The PT-JPL<sub>SM</sub> introduced a constraint (0–1,  $C_{RSM}$ ) of surface SM for T and E,  
 190 which was used to avoid the implicit soil water control (represented by  $f_{SM}=RH^{VPD}$ ) in the PT-JPL model.

191 Vegetation transpiration:

$$192 C_{RSM} = (1 - RH^{4(1-VWC)(1-RH)})C_{SM} + (RH^{4(1-VWC)(1-RH)})C_{TRSM} \quad (2.5)$$

$$C_{\text{TRSM}} = 1 - \left( \frac{W_{\text{CR}} - W_{\text{obs}}}{W_{\text{CR}} - W_{\text{pwp\_CH}}} \right)^{\sqrt{\text{CH}}}, \quad (2.6)$$

where  $w_{\text{obs}}$  is the SMAP SM,  $w_{\text{pwp}}$  is the water content at the wilting point, and  $w_{\text{fc}}$  is the water content at field capacity, which is determined by the properties of the soil.  $W_{\text{CR}}$  is a crucial parameter in characterizing the extent of SM restriction on ET;  $w_{\text{pwp\_CH}}$  is the canopy height (CH) and is related to the potential of roots capturing water from deeper sources to limit the transpiration rate and characterize the SM availability (Purdy et al., 2018; Evensen 2003; Serraj et al., 1999). The specific formula is given in Purdy et al. (2018).

Soil evaporation:

$$C_{\text{RSM}} = \frac{W_{\text{obs}} - W_{\text{pwp}}}{W_{\text{fc}} - W_{\text{pwp}}} \quad (2.7)$$

The proportion of available water limits the soil evapotranspiration to the maximum available water. This scalar was formulated to represent the relatively accurate extractable water content for the vegetation, determined by soil properties and the water available for evaporation, which is estimated via surface water constraints.

The SMAP SM as surface SM data was applied to model global ET using PT-JPL<sub>SM</sub> and the results demonstrated the largest improvements for ET estimates in dry regions (Purdy et al. 2018). Due to the limitation of soil stratification in LPJ-DGVM, the model was coupled with an updated remote-sensing

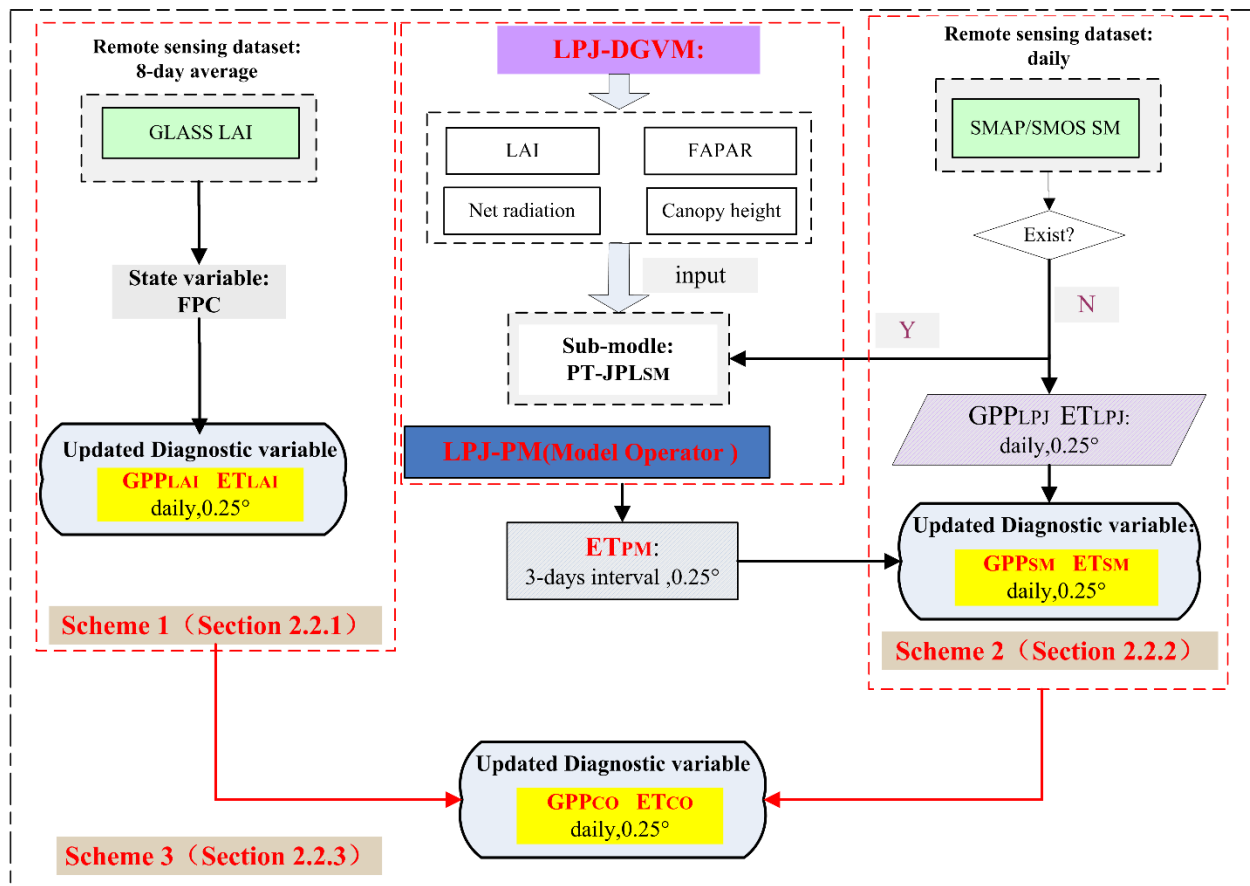
209 ET algorithm in the PT-JPL<sub>SM</sub> that could better simulate ET in water-limited regions than in humid regions  
210 (Purdy et al. 2018).

## 211 *2.2. Assimilation scheme and experiment procedure*

212 To improve the prediction capability of LPJ-PM, we designed three assimilation schemes:  
213 assimilating LAI only (scheme 1, **output: ET<sub>LAI</sub>, GPP<sub>LAI</sub>**), assimilating SSM only (scheme 2, **output:**  
214 **GPP<sub>SSM</sub>, ET<sub>SSM</sub>**), and joint assimilation of LAI and SSM (scheme 3, **output: ET<sub>CO</sub>, GPP<sub>CO</sub>**), i.e., LPJ-  
215 VSJA framework) to test the assimilation performance for simulating GPP and ET.

216 The proposed LPJ-VSJA framework consists of four main components: the model operator (the LPJ-  
217 PM), the observation operator (to establish the relation between the assimilation variable and the observed  
218 variable), the observation series (GLASS LAI and SMOS or SMAP products), and the assimilation  
219 algorithm (POD4DVar). With the surface soil moisture constraint in the PT-JPL<sub>SM</sub>, the LPJ-VSJA  
220 corrects the output fluxes (GPP and ET in this study).

## LPJ-VSJA assimilation system



221

222

223

224

225

226

**Figure 1. Flowchart of the LPJ-VSJA assimilation scheme: three assimilation schemes and the coupled model: LPJ-PM. (adapted from Li et al., 2020). The abbreviation of model and assimilation framework is explained in Table 1.**

The experiment consisted of six steps:

227 Step 1: initialize the LPJ-DGVM and output the reference state variables without assimilation over  
228 the experimental period (2010–2018), referred to as the “Control run” scenario.

229 Step 2: implement schemes 1, 2, and 3, respectively, and the results represent the assimilation  
230 integration state (daily GPP and ET assimilation results are referred to as the “GPP<sub>LAI</sub>” and “ET<sub>LAI</sub>” in  
231 scheme 1; “GPP<sub>SM</sub>” and “ET<sub>SM</sub>” in scheme 2 and “GPP<sub>CO</sub>” and “ET<sub>CO</sub>” in scheme 3. This scenario used  
232 the same input data and model parameter scheme with the “Control run” scenario.

233 Step 3: evaluate GPP and ET results (schemes 1, 2 and 3 ) by comparing the parameters,  $R^2$   
234 (correlation coefficient), BIAS, and ubRMSD (unbiased root mean square deviation), for conditions of  
235 without-DA (“Control run” scenario) and with-DA states, and assess the assimilation performance of  
236 separate assimilation (schemes 1 and 2) and joint assimilation (scheme 3) to determine the optimal  
237 assimilation scheme for GPP and ET, respectively.

238 Step 4: evaluate the in-situ assimilated GPP and ET results where the sites are located in wet or dry  
239 regions by dividing these validation sites into four parts (humid, sub-dry humid, semi-arid, and arid  
240 regions), and this step was designed to assess the superiority of the proposed assimilation scheme in  
241 water-limited areas.

242 Step 5: compare the ET assimilation performance by assimilating the SMOS data with that by  
243 assimilating the SMAP data.

244 Step 6: evaluate the simulated GPP and ET maps based on the optimal assimilation scheme against  
245 existing global flux products.

### 2.2.1 DA scheme 1: LAI assimilation

In assimilation scheme 1, the observation operator determines the relationship between LAI and foliage projective cover (FPC) in the process model (equation 2.1), and the assimilated LAI will be propagated by energy transmission and ecosystem processes (e.g. photosynthesis, transpiration of vegetative process) in the dynamic model to improve GPP and ET simulations (Bonan et al. 2014; Mu et al. 2007). FPC, the vertically projected percentage of the land covered by foliage, regulates the rate of photosynthate conversion and transpiration. In this study, the GLASS LAI with 8-day interval for the period 2010–2018 was selected as the observation dataset for assimilation, and the FPC state variable was updated daily through running the LPJ-PM ( $GPP_{LAI}$ ,  $ET_{LAI}$  in this study) as shown below:

$$FPC = 1 - e^{-0.5LAI} \quad (2.1)$$

We set the model and observation errors at a given time as 20% and 10% (scale factor) of the LAI value and the observed LAI value, respectively. By verifying the assimilation performance (R, RMSD, BIAS) for different scale factors (f) of model simulation and observations in the range of 0.05 to 0.40, taking a step size of 0.05 (a total of 64 combinations), the optimal scale factors (0.2 and 0.1) were determined (Bonan et al., 2020). The model and observation errors was the LAI value multiply by f. The model integration generation method described by Pipunic et al. (2008) was used to determine the minimum number of ensemble members required to achieve maximum efficiency, and the number of sets was 20.

### 2.2.2 DA scheme 2: SSM assimilation



265 In this scheme, the surface SM products (SMOS or SMAP) were assimilated to LPJ-PM to obtain  
266 more accurate ET ( $ET_{SM}$ ) estimates in water-limited areas. The observation series was the SMOS or  
267 SMAP SSM product, and the observation operator was the PT-JPL<sub>SM</sub> model. The  $ET_{PM}$  estimated by the  
268 coupled model (LPJ-PM) introducing surface SM was directly assimilated as a diagnostic variable. The  
269 assimilated ET was applied to compute the top layer SM (50 cm) at the next time step (a nonlinear soil  
270 water availability function described by Zhao et al. (2013), providing feedback for subsequent hydrologic  
271 and carbon cycle processes. Then, the updated SM values regulated the GPP simulation (output:  $GPP_{SM}$ ).  
272 Different from other "constant" ET observations, the  $ET_{PM}$  ("observation") at each time  $t$  were adjusted  
273 by absorbing intermediate variables updated after assimilation at time  $t-1$ . The  $ET_{PM}$  was shown to be  
274 better than ET simulated by LPJ-DGVM but not as good as that simulated by the model with SMAP SM  
275 assimilated (Li et al. 2020). Thus, it is proven that this SM assimilation schemes could improve the  
276 accuracy of ET simulations.

277 All assimilation simulations were conducted between January 2010 and December 2018. Between  
278 January 2010 and April 2015, SMOS data were used for assimilation; and after May 2015, both SMOS  
279 and SMAP data were used for assimilation. An assimilation scheme was conducted when RH and SMOS  
280 or SMAP SM data existed simultaneously; otherwise, the original simulation of the LPJ-DGVM was  
281 conducted directly without adjustment of assimilation.

282 Similar to the LAI assimilation scheme, the model and observation errors were set as 15% and 5%  
283 of  $ET_{LPJ}$  and  $ET_{PM}$ , respectively (LPJ-PM was adopted before assimilation). The number of ensemble

284 members was set to 50. The  $ET_{PM}$  must be rescaled to the  $ET_{LPJ}$  distribution via their corresponding  
285 cumulative probabilities using the cumulative distribution function (CDF) matching to avoid introducing  
286 any bias in the LPJ-VSJA system (Li et al. 2020).

### 287 2.2.3 DA scheme 3: joint assimilation of LAI and SSM

288 In this scheme, both LAI from GLASS and SM from SMOS or SMAP were the observation datasets.  
289 The GLASS LAI was assimilated by scheme 1 to obtain the  $FPC_{DA}$  and  $ET_{LAI}$ , and then the  $FPC_{DA}$  served  
290 as input to LPJ-PM to simulate optimized  $ET_{PM}$ , and the  $ET_{LAI}$  was further assimilated with  $ET_{PM}$  to  
291 generate  $ET_{CO}$ . Then, the SM (referred to as  $SM_{CO}$  in Figure S1) updated by  $ET_{CO}$  and the  $FPC_{DA}$  were  
292 used as input to correct GPP ( $GPP_{CO}$ ).

293 Here, we applied the error regulation in scheme 1 and maintained the error setting of the LAI  
294 observation and model simulation. Considering the transmission of integrated model error, we  
295 recalculated the model error of LPJ-PM after the LAI assimilation and set model and observation errors  
296 of  $ET_{LAI}$  and  $ET_{PM}$  to be 15 and 10%, respectively.

### 297 2.3. *POD-Based Ensemble 4D Variational Assimilation Method*

298 The Proper Orthogonal Decomposition (POD)-based ensemble four-dimensional variational (4DVar)  
299 assimilation method (referred to as  $POD_{En}4DVar$ ) ([Tian and Feng 2015](#)) has the advantage of avoiding  
300 the calculation of adjoint patterns as its incremental analysis field, which can be represented linearly by  
301 the POD base (Transformed OP (Observing Perturbation) and MP (Model Perturbation)). Moreover, the

302 PODEn4DVar can simultaneously assimilate multiple-time observation data and provide flow-dependent  
 303 (the flow-dependent is the ensembles of forecasting statistical characteristics in the t time) error estimates  
 304 of the background errors. It has shown advantages in terrestrial assimilation, Tan-Tracker joint DA, and  
 305 Radar assimilation (Tian et al. 2010; Tian et al. 2009; Tian et al. 2014; Zhang and Weng 2015).

306 By minimizing the following initial incremental format of the cost function in the 4DVar algorithm,  
 307 an analysis field can be obtained:

$$308 \quad J(\mathbf{x}') = \frac{1}{2}(\mathbf{x}')\mathbf{B}^{-1}(\mathbf{x}') + \frac{1}{2}[\mathbf{y}'(\mathbf{x}') - \mathbf{y}'_{obs}]^T \mathbf{R}^{-1}[\mathbf{y}'(\mathbf{x}') - \mathbf{y}'_{obs}]$$

309 Here, the  $\mathbf{x}' = \mathbf{x} - \mathbf{x}_b$ ,  $\mathbf{y}'(\mathbf{x}') = \mathbf{y}(\mathbf{x}' + \mathbf{x}_b) - \mathbf{y}(\mathbf{x}_b)$ ,  $\mathbf{y}'_{obs} = \mathbf{y}_{obs} - \mathbf{y}(\mathbf{x}_b)$ ,  $\mathbf{y} = \mathbf{H}[\mathbf{M}_{t_0 \rightarrow t_k}(\mathbf{x})]$ .  
 310  $\mathbf{x}'(\mathbf{x}'_1, \mathbf{x}'_2, \dots, \mathbf{x}'_N)$  is the model perturbation (MP) matrix and  $\mathbf{y}'(\mathbf{y}'_1, \mathbf{y}'_2, \dots, \mathbf{y}'_N)$  is the  
 311 observation perturbation (OP) matrix with N samples. Following Rüdiger et al. (2010), the LAI  
 312 perturbation was set to a fraction (0.001) of the LAI itself. The perturbation of ET<sub>PM</sub> and ET<sub>LPI</sub> conforms  
 313 to a Gaussian distribution with a mean of 0 and a specified covariance (10 and 5% of the ET<sub>PM</sub> and ET<sub>LPI</sub>  
 314 at time t). The subscript b represents the background field, the superscript T represents a transpose, H is  
 315 the observation operator of scheme 1 as described in section 2.2.1, and scheme 2 is the PT-JPL<sub>SM</sub>  
 316 (described in 2.1.2). M is the forecast model (LPJ-PM in this study), B is the background error covariance,  
 317 R is the observation error covariance, and obs denotes observation.

318 Assuming the approximately linear relationship between OP(y') and MP(x'), POD decomposition  
 319 and transformation were successively conducted for OP and MP. The transformed OP samples ( $\Phi_y =$

320  $y'_1, y'_2, \dots, y'_n$ ) are orthogonal and independent, and the transformed MP samples ( $\Phi_x =$   
 321  $x'_1, x'_2, \dots, x'_n$ ) are orthogonal to the corresponding OP samples, where n is the number of POD modes.

322 The manifestation of the background error covariance is the same as the Ensemble Kalman filter  
 323 (EnKF, Evensen (2004)), and the incremental analysis  $x'_a$  was expressed by the  $\Phi_{x,n}$ , and  $\tilde{\Phi}_y$  ( $\tilde{\Phi}_y =$   
 324  $[(n-1)I_{n \times n} + \Phi_{y,n}^T R^{-1} \Phi_{y,n}]^{-1} \Phi_{y,n}^T R^{-1}$ ). Finally, the optimal analysis  $x_a$  is calculated as  $x_a = x_b +$   
 325  $\Phi_{x,n} \tilde{\Phi}_y y'_{obs}$ . The detailed derivation process of the algorithm is described by a previous study (Tian et  
 326 al. 2011).

327 In the ensemble-based method (Evensen et al., 2004), the number of ensemble members is usually  
 328 fewer than that of the observation data and the degrees of freedom of the model variables, and spurious  
 329 long-range correlations occur between observation locations and model variables. A practical method, the  
 330 localization technique, is applied to address this issue (Mitchell et al. 2002). The final incremental analysis  
 331 is rewritten as:

$$332 \quad x'_a = \Phi_{x,n} \tilde{\Phi}_y y'_{obs} C_0 \left( \frac{d_h}{d_{h,0}} \right) \cdot C_0 \left( \frac{d_v}{d_{v,0}} \right)$$

333 where  $d_h$  and  $d_v$  are the horizontal and vertical distances between the spatial positions of state and  
 334 observed variables, respectively; and  $d_{h,0}$  and  $d_{v,0}$  are the horizontal and vertical covariance localization  
 335 Schur radii, respectively. The filtering function  $C_0$  is expressed as:

$$C_0(r) = \begin{cases} -\frac{1}{4}r^5 + \frac{1}{2}r^4 + \frac{5}{8}r^3 - \frac{5}{3}r^2 + 1, & 0 \leq r \leq 1, \\ \frac{1}{12}r^5 - \frac{1}{2}r^4 + \frac{5}{8}r^3 + \frac{5}{3}r^2 - 5r + 4 - \frac{2}{3}r^{-1}, & 1 \leq r \leq 2, \\ 0, & 2 < r \end{cases}$$

where  $r$  is the radius of the filter.

The assimilation algorithm is mainly divided into two steps: (1) prediction: run LPJ-PM in the current assimilation window and generate simulation results and background field vectors; (2) update: the algorithm is used to calculate the optimal assimilation increment  $x'_a$  and analysis solution  $x_a$ , and the simulation results and the initial conditions of the model in the current window are updated using the analysis solution. The updated initial conditions were applied for model LPJ-PM prediction, and the above process was repeated.

#### 2.4. Validation method for assimilation performance

The  $R^2$  (correlation coefficient), Bias, and ubRMSD (unbiased root mean square deviation) between simulation and tower-based observations were applied for evaluation. In addition, a Taylor chart was also used to demonstrate the performance of two ET estimations with different SM observations in terms of  $R$ , ubRMSD, and Normalized Standard Deviation (NSD) on 2D plots, to display how closely the datasets matched observations in one diagram (Taylor 2001). In the Taylor diagram, SD represents the radial distance from the origin point and the correlation with the site observations as an angle in the polar plot. The ubRMSD is the distance between the observation and the model and is represented in the figure as a green semi-circular arc with point A as the center of the circle. The closer the model point to the

353 reference point (Point A), the better the performance. This diagram is convenient and visual in evaluating  
354 multiple aspects of various models.

355 The error variance of GPP and ET products was estimated using the triple collocation (TC) approach  
356 (Stoffelen 1998) to validate the global simulation in this study. The method has been extensively applied  
357 in the study of hydrology and oceanography (Caires and Sterl 2003; Khan et al. 2018; O'Carroll et al.  
358 2008; Stoffelen 1998), particularly in SM studies (Chan et al. 2016; Kim et al. 2018). The TC provides a  
359 reliable platform for comparison of spatial assimilation results and in-situ measurements. In this  
360 experiment, no calculation was performed on the non-vegetated areas where the correlation was lower  
361 than 0.2 to have independent datasets and avoid correlated errors (crucial assumptions in TC) (Yilmaz  
362 and Crow 2014).

363 In this study, the five products were divided into three product categories, including satellite product  
364 (MODIS, GOSIF GPP), reanalysis product (GLASS, GLDAS) and data assimilation product (GLEAM  
365 ET, LPJ-VSJA) (Li et al.,2018). One product in each category was selected to form a group to calculate  
366 their error. The LPJ-VSJA product was set as the reference data.

367 For GPP products, GOSIF, GLASS, and LPJ-VSJA were treated as a group, and MODIS, GLASS  
368 and LPJ-VSJA were treated as another group to calculate the errors; the final errors were determined by  
369 the average of these two.

370 **3. Similarly, to calculate the errors for ET, GLEAM, GLASS, and MODIS were chosen as a**  
371 **group; LPJ-VSJA, GLDAS, and MODIS were treated as a group; LPJ-VSJA, GLASS and**

372 **MODIS were considered as a group. In order to reduce the influence of orthogonality**  
373 **hypothesis of error, the first and third groups are for indirect and effective comparison**  
374 **between LPJ-VSJA product and GLEAM product. Experiment sites and data**

### 375 *3.1. Description of flux tower sites*

376 We screened over 300 EC flux sites across the globe from the FLUXNET2015  
377 (<https://fluxnet.fluxdata.org/data/fluxnet2015-dataset/>), AmeriFlux (<http://public.ornl.gov/ameriflux/>),  
378 and the HeiHe river basin (Liu et al. (2018), <http://www.heihedata.org/>) for the evaluation of assimilation  
379 performance over the period from January 2010 to December 2018. The in-situ half-hourly LE and GPP  
380 data from the sites were aggregated into daily data. The daily gap-filled data were excluded if the  
381 percentage of gap-filled half-hourly values was more than 20%. Then we corrected the data of energy  
382 non-closure by using the Bowen ratio closure method (Twine et al. 2000) to improve the energy closure  
383 rate (Huang et al. 2015; Yang et al. 2020). The data were selected to cover the 2010–2018 period with at  
384 least one year of reliable data, and the result from the error of assimilation is relative to the LE value and  
385 seasonal variation (Purdy et al. 2018; Zou et al. 2017). It is essential to have available data every month  
386 during a one-year period, and only days with less than 25% missing data were processed per month (Feng  
387 et al. 2015). In addition, for flux tower data, the data were also excluded for the analysis if the  
388 SMAP/SMOS SM data were not of good quality.

389 Finally, we identified a total of 105 sites across the globe encompassing five major biomes: grassland  
390 (18 for GPP and 19 for ET), savanna (11), shrubland (4), forest (49 and 53), and cropland (13 and 14). In

391 the comparative analysis of the performance for simulating ET by assimilating SMOS and SMAP SM  
392 data separately, we selected 46 AmeriFlux sites (Figure S3) with at least one year of reliable data from  
393 2015 to 2018 based on the simultaneous availability of SMAP and SMOS data, including grassland (19),  
394 savanna (11), shrubland (5), forest (23), and cropland (7). Figure S2 and S3 illustrate the location and  
395 distribution of the 105 and 46 EC flux tower sites, respectively. A more detailed description is  
396 summarized in the Supporting Information Table S1.

### 397 *3.2. Remote sensing datasets: LAI and SM*

398 The GLASS LAI product with an 8-day time step and 5 km resolution was derived from MODIS  
399 and CYCLOPES surface reflectance and ground observations using general regression neural networks  
400 (GRNNs) (Liang et al. 2013; Xiao et al. 2016). The verification of the product using the mean values  
401 of high-resolution LAI maps showed that the GLASS LAI values were closer to these high-resolution  
402 LAI maps (RMSD= 0.78 and  $R^2= 0.81$ ). Therefore, the GLASS LAI product has satisfactory performance  
403 and can be assimilated into terrestrial biosphere models.

404 The SMAP mission (Entekhabi et al. 2010) and SMOS mission (Jacquette et al. 2010), the two  
405 dedicated soil moisture satellites currently in orbit equipped with L-band microwave instruments, provide  
406 surface SM retrievals. We chose the SMOS-L2 product and the SMAP-L3-Enhanced product, which both  
407 provide global coverage every three days for soil depth of 5 cm. Only good-quality SMAP and SMOS  
408 data were used. The grid cells with water areas larger than 10% and those with less than 50% good-quality  
409 data in one year were masked out, which alleviates the undesirable model simulations caused by the



410 decrease in SMAP retrieval accuracy (Chan et al. 2016; O'Neill et al. 2010). We only adopted the data  
411 with an uncertainty below  $0.1 \text{ m}^3 \text{ m}^{-3}$ , in the actual range (0.00– $0.6 \text{ m}^3 \text{ m}^{-3}$ ), and the temperature of the  
412 LSM observation layer (the second layer) was higher than  $2 \text{ }^\circ\text{C}$  (Blyverket et al. 2019).

413 Both the GLASS LAI, SMOS and SMAP observations was resampled to 9 km for site simulation  
414 and  $0.25^\circ$  for spatial simulation.

### 415 3.3. Model-forcing and validation datasets

416 In this study, the meteorological, soil property, and  $\text{CO}_2$  concentration datasets were used to drive  
417 the LPJ-PM. For site simulation, in order to maintain consistency with the SMAP Enhanced 3 Level  
418 product (Entekhabi et al. 2010), model-forcing data were resampled to a 9 km spatial resolution based on  
419 EASE-2 projection grid. In the global spatial simulation, the model-forcing datasets were interpolated to  
420  $0.25^\circ$  based on the bilinear method to ensure the consistency of spatial representation. Table 2 provides  
421 the spatial and temporal characteristics of the model-forcing datasets in the LPJ-PM (submodule: LPJ-  
422 DGVM and PT-JPL<sub>SM</sub>).

423

424 **Table 2. List of the selected forcing and remote-sensing datasets used in this study**

Datasets	Variable	Period	Spatial resolution	References
CRU TS v4.1 <sup>a</sup>	Cloud cover,	1901-	$0.5^\circ \times 0.5^\circ$	New et al.

	temperature, precipitation, wet day	1930		(2000), <a href="https://crudata.uea.ac.uk/cru/data/hrg/">https://crudata.uea.ac.uk/cru/data/hrg/</a> (Etheridge et al. (1996); Keeling et al. (1995)), <a href="https://scrippsco2.ucsd.edu/data/atmospheric_co2/">https://scrippsco2.ucsd.edu/data/atmospheric_co2/</a>
Ice-core measurements and atmospheric observations at the Mauna Loa Observatory <sup>a</sup>	Atmospheric CO <sub>2</sub> concentrations	1901- 2018	NA	Rienecker et al. (2011) ( <a href="https://www.esrl.noaa.gov/pds/">https://www.esrl.noaa.gov/pds/</a> ) Wieder et al. (2014) ( <a href="http://daac.ornl.gov">http://daac.ornl.gov</a> )
MERRA-2 <sup>a</sup>	Precipitation, surface temperature, cloud fraction, relative humidity	2010- 2018	0.5° × 0.625°	
HWSD (v121) <sup>b</sup>	Soil texture data	NA	1 km × 1 km	

SPL3SMP_E <sup>b</sup>	Surface soil moisture	2015.4– present	9 km×9 km	Entekhabi et al. (2010), ( <a href="https://smap.jpl.nasa.gov/">https://smap.jpl.nasa.gov/</a> )
GLASS LAI <sup>a,b</sup>	Leaf area index	2010- 2018	5 km×5 km	Xiao et al. (2016), ( <a href="http://www.glass.umd.edu/Download.html">http://www.glass.umd.edu/Download.html</a> )
SMOS_L3 CATDS <sup>b</sup>	Surface soil moisture	2010- present	25km×25 km	Jacquette et al. (2010), ( <a href="https://earth.esa.int/eogateway/missions/smos">https://earth.esa.int/eogateway/missions/smos</a> )

---

<sup>a</sup>: forcing dataset for LPJ-DGVM

<sup>b</sup>: external input dataset for PT-JPL<sub>SM</sub>

425

426

427

428 We used four global ET products and three global GPP products (Li et al. 2018; Li and Xiao 2019;  
 429 Wang et al. 2017) that was resample to  $0.25^\circ$  to evaluate the performance of the model with the joint  
 430 assimilation scheme. Table 3 shows the details of these GPP and ET products.

431 **Table 3. Global GPP and ET products for comparison in this study**

Product	Dataset	Temporal resolution	Spatial resolution	Retrieval algorithm	References
MOD17A2	GPP and ET	8-day average	$1 \text{ km} \times 1 \text{ km}$	GPP: Based on the light use efficiency (LUE) model ET: Improved Penman formula	Running et al. (2004)
GLASS	GPP and ET	8-day average	$5 \text{ km} \times 5 \text{ km}$	GPP: EC-LUE model ET: Combining five Bayesian averages based on process models (BMA)	Yuan et al. (2010)
GOSIF GPP	GPP	8-day average	$0.05^\circ \times 0.05^\circ$	Estimated from solar-induced chlorophyll	Li and Xiao (2019)

---

				fluorescence with GPP-	
				SIF relationships	
GLDAS ET	ET	daily	0.25°× 0.25°	Processed model assimilation	Fang et al. (2009)
GLEAM v3a ET	ET	daily	0.25°× 0.25°	Processed model assimilation	Martens et al. (2017)

---

432

## 433 4. Results

### 434 4.1. Performance of LPJ-PM for simulating GPP and ET with the assimilation of LAI and soil moisture

#### 435 4.1.1 Accuracy assessment of GPP for separate and joint assimilation

436 In general, the  $R^2$  between  $GPP_{LPJ}$  and  $GPP_{OBS}$  was above 0.4 at most of the sites (62 sites) and  
437 were relatively weak for some sites. The LAI assimilation improved the simulations at most sites ( $R^2$   
438 value increased at 82 sites), particularly for sites in the U.S. and Europe (Figure 2). The  $R^2$   
439 improvement from the LAI assimilation (scheme 1) was superior to that from the SM assimilation  
440 (Figure 2- $R^2$  (b) and (c)). The performance of the joint assimilation (scheme 3) was similar to that of  
441 scheme 1. . Sites (Figure 2-BIAS (a)) showed positive bias ( $GPP_{OBS}-GPP_{LPJ}$ ) were mainly distributed in  
442 the humid and dry-sub humid forest, grassland, and arid cropland regions, showing an underestimation  
443 for  $GPP_{OBS}$ . The assimilation improved the accuracy for overestimated sites, but there was no

444 significant improvement for underestimated sites. The ubRMSD implied that the SM assimilation alone  
445 had a better performance than the LAI assimilation alone, especially for sites in arid areas. The analysis  
446 of the above three statistical measures ( $R^2$ , BIAS, and ubRMSD) indicated that the accuracy of joint  
447 assimilation was much better than that of separate assimilation.

448 At the seasonal scale, all three assimilation schemes corrected the model trajectory and  
449 significantly improved the growing season simulations, especially for peak values (IT-Tor, US-NR1,  
450 US-NE1)(Figure 3). In addition, the linear fitting of  $GPP_{CO}$  and  $GPP_{OBS}$  on a monthly scale was closer  
451 to 1:1 ( $y = 0.92 + 21.66 p < 0.001$ ) than that of  $GPP_{LAI}$  ( $y = 0.89 + 28.3, p < 0.001$ ) and  $GPP_{SM}$  ( $y = 0.86$   
452  $+ 41.70, p < 0.001$ ) (Figure S5). The results in Table S2 support the above analysis, and the joint  
453 assimilation showed advantages in overall accuracy in both arid and humid areas.

454

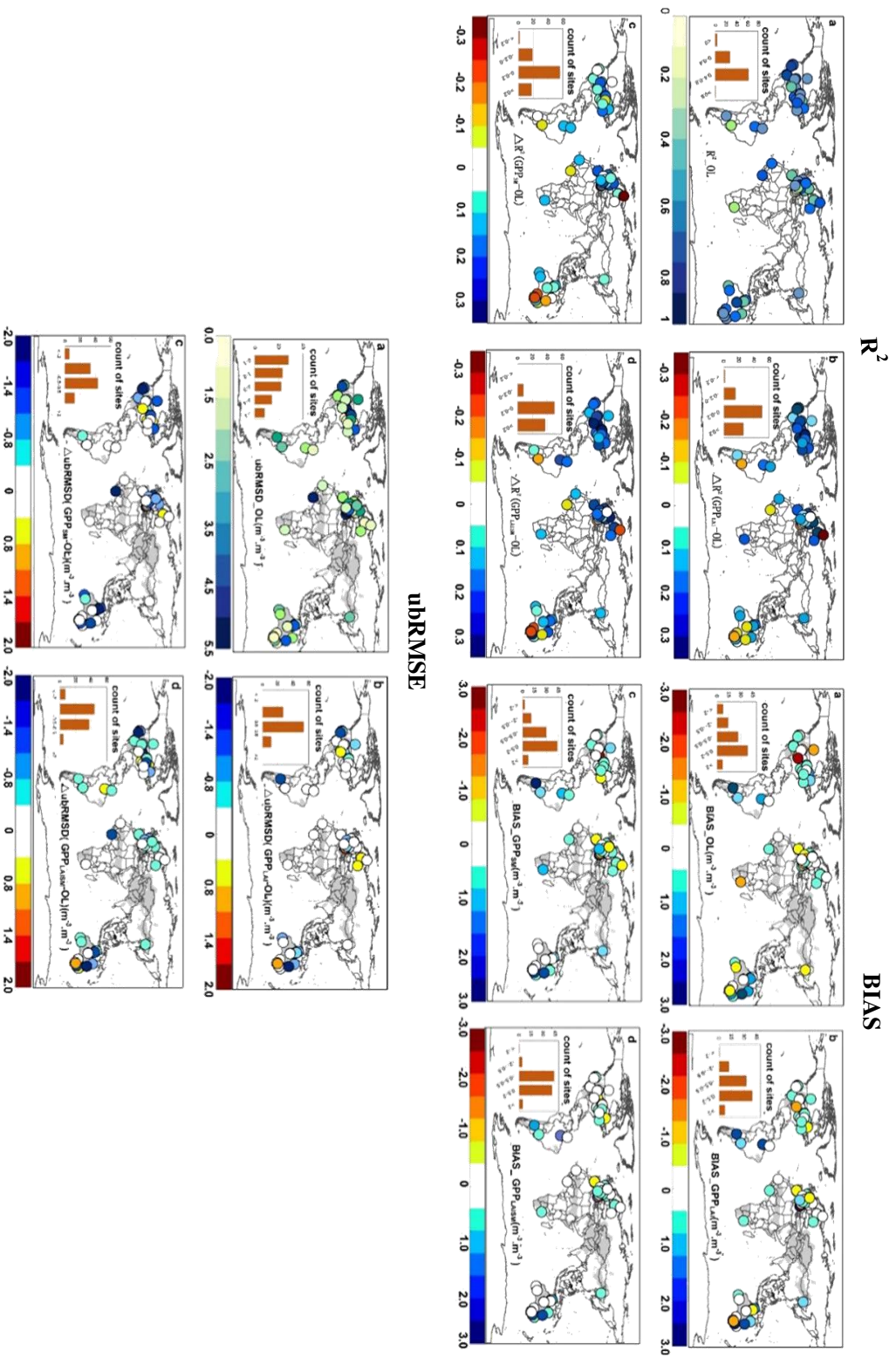
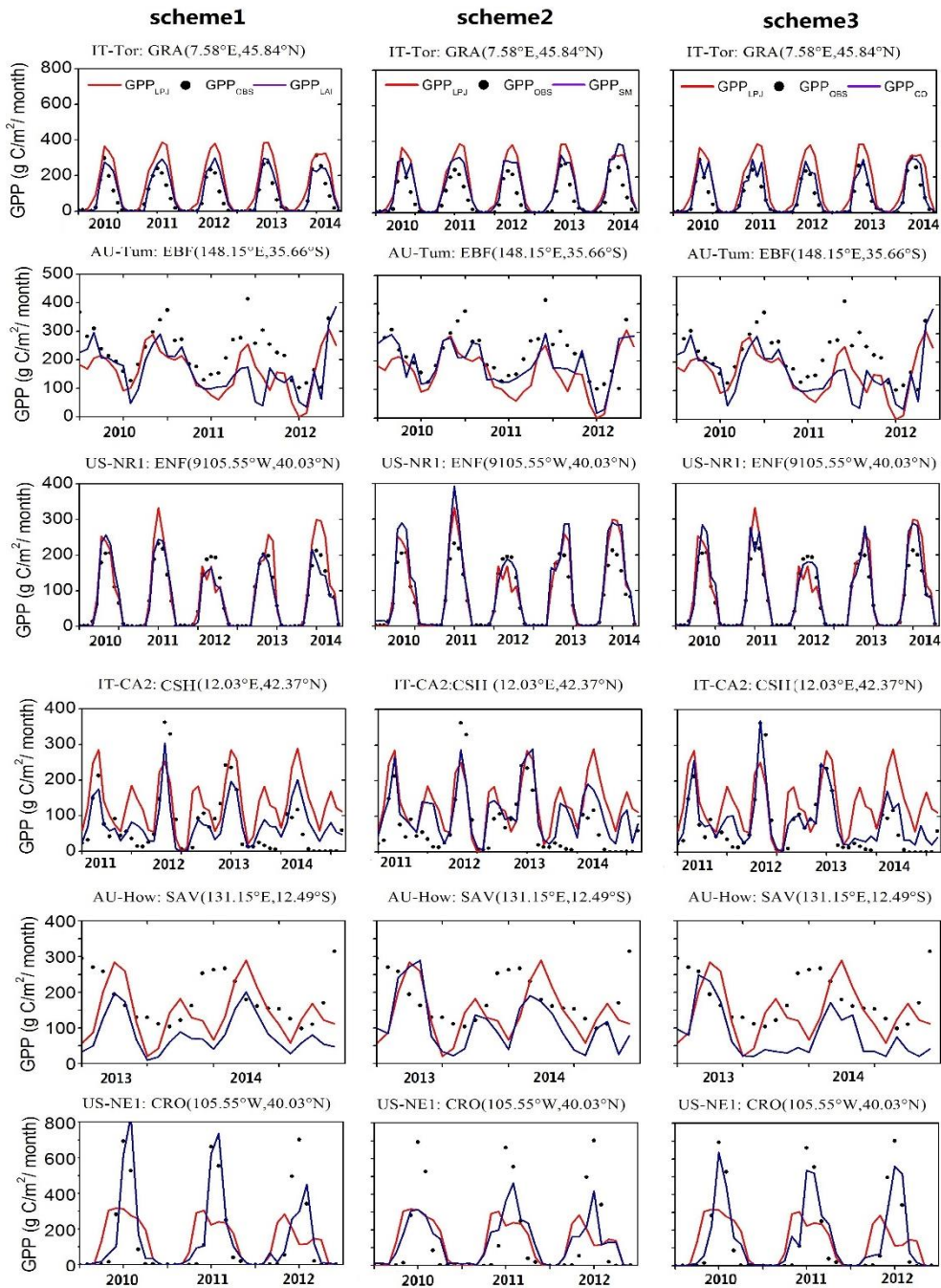


**Figure 2** (a) The correlation coefficient ( $R^2$ ), Bias and the Unbiased Root Mean Square Error (ubRMSE) between the  $GPP(GPP_{LAI})$  simulated by the LPJ-DGVM and the site observations, the yellow/blue indicating low/high correlation ; (b)  $\Delta$

$R^2$ (correlation difference between  $GPP_{LAI}$  and  $GPP_{LPJ}$ ), BIAS ( $GPP_{LAI}$ ) and  $\Delta$ ubRMSE ( $GPP_{LAI}$ -  $GPP_{LPJ}$ ) ;(c)  $\Delta R^2$  (correlation

difference between  $GPP_{SM}$  and  $GPP_{LPJ}$ ) ,  $\Delta$  BIAS ( $GPP_{SM}$ ) and  $\Delta$ ubRMSE ( $GPP_{SM}$ -  $GPP_{LPJ}$ ) ; (d)  $\Delta R^2$  (The correlation

difference between  $GPP_{CO}$  and  $GPP_{LPJ}$ ) ,  $\Delta$  BIAS ( $GPP_{CO}$ ) and  $\Delta$ ubRMSE ( $GPP_{CO}$ -  $GPP_{LPJ}$ ) , blue/red represent positive/negative values.



456

457

458

**Figure 3. Seasonal cycles of tower GPP and simulated gross primary productivity (GPP) from Lund-Potsdam-Jena (LPJ), GLASS LAI assimilation (scheme 1), SMOS assimilation (scheme 2) and joint**



assimilation (scheme 3) for six sites representing six PFTs.

The residual analysis indicated that the three assimilation schemes for GPP (Figure S7 (left)) were different. For the assimilation results, most of the errors were distributed around  $-70 \sim 60 \text{ g C m}^{-2} \text{ month}^{-1}$ . The high  $\text{GPP}_{\text{OBS}}$  values were considerably underestimated. The maximum negative error reached  $100 \text{ g C m}^{-2} \text{ month}^{-1}$ . The error distribution of  $\text{GPP}_{\text{SM}}$  was more dispersed than that of  $\text{GPP}_{\text{LAI}}$  and  $\text{GPP}_{\text{CO}}$ . Among the residuals of these three schemes,  $\text{GPP}_{\text{SM}}$  significantly overestimated the  $\text{GPP}_{\text{OBS}}$ , mainly distributed in the  $0\text{--}200 \text{ g C m}^{-2} \text{ month}^{-1}$  range.  $\text{GPP}_{\text{LAI}}$  showed significant improvement in the overestimation of  $\text{GPP}_{\text{OBS}}$  compared with  $\text{GPP}_{\text{CO}}$ . In general, the  $\text{GPP}_{\text{CO}}$  with the most concentrated error distribution had significant improvement.

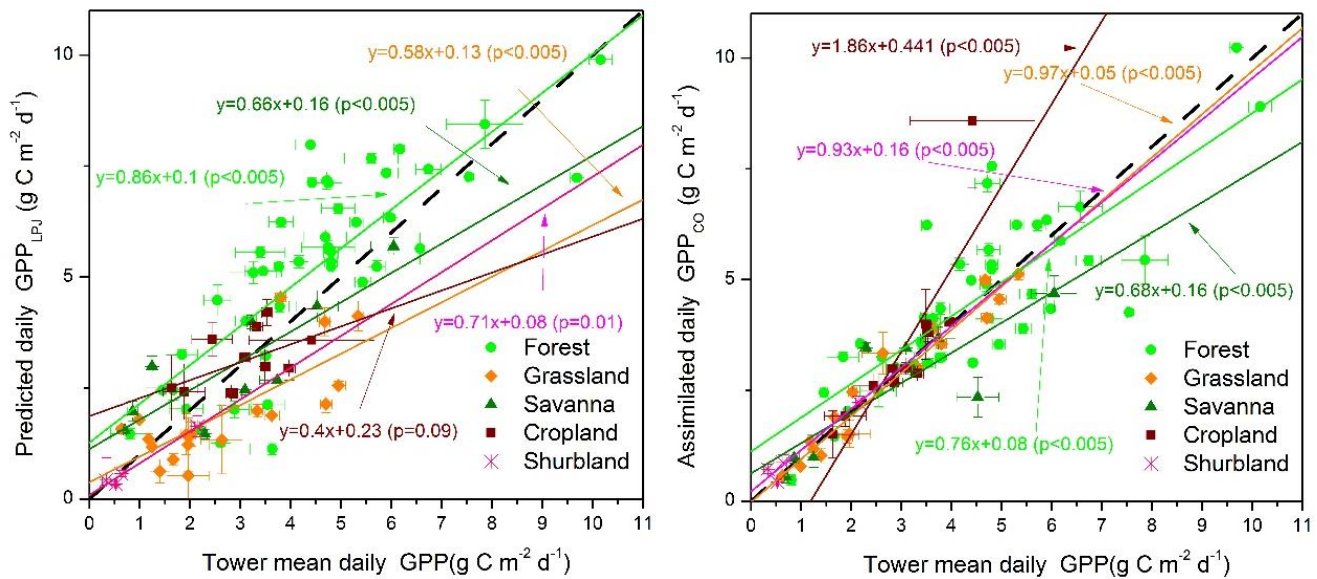


Figure 4. Scatterplots of daily  $\text{GPP}_{\text{LPJ}}$  (left) and  $\text{GPP}_{\text{CO}}$  (right) versus tower GPP for different PFTs.

After determining the optimal assimilation scheme (scheme 3), we evaluated the  $\text{GPP}_{\text{LPJ}}$  and  $\text{GPP}_{\text{CO}}$

471 at the site level (Fig.4). The results showed that  $GPP_{CO}$  performed better ( $R^2= 0.83$ ,  $ubRMSD= 1.15 \text{ g C}$   
472  $\text{m}^{-2} \text{ d}^{-1}$ ) than  $GPP_{LPJ}$  ( $R^2= 0.69$ ,  $ubRMSD= 1.91 \text{ g C m}^{-2} \text{ d}^{-1}$ ). The noticeable underestimation in all PFTs  
473 and overestimation at most forest sites for  $GPP_{LPJ}$  were corrected by joint assimilation ( $GPP_{CO}$ ). Our joint  
474 assimilation methods had better performance in forests, shrublands, and grasslands than in croplands and  
475 savannas. Except for the cropland, the linear fitting results of other types were all below the 1:1 line,  
476 showing the overall underestimation. Superior performance in both original simulation and assimilation  
477 occurred at shrubland ( $R^2= 0.93$ ,  $ubRMSD= 0.89 \text{ g C m}^{-2} \text{ d}^{-1}$ ) and grassland ( $R^2= 0.97$ ,  $ubRMSD= 0.83$   
478  $\text{g C m}^{-2} \text{ d}^{-1}$ ) sites. However, the standard deviation of  $GPP_{CO}$  and  $GPP_{OBS}$  at savanna sites was relatively  
479 large, and the assimilated GPP at several savanna sites was significantly underestimated.

#### 480 4.1.2 Accuracy assessment of ET for separate and joint assimilation

481 In general, the coefficient of determination ( $R^2$ ) between  $ET_{LPJ}$  and  $ET_{OBS}$  was generally over 0.4  
482 (the simulations were superior to  $GPP_{LPJ}$ ) (Figure 5).  $ET_{LAI}$  showed slightly higher  $R^2$ , while some sites  
483 showed reduced values (41 sites). The  $ET_{SM}$  and  $ET_{CO}$  were significantly improved compared with the  
484  $ET_{LAI}$ . The  $R^2$  increased considerably in Australia but declined at some sites in the United States after  
485 assimilation. For  $ubRMSD$ ,  $ET_{CO}$  performed better than  $ET_{SM}$  and  $ET_{LAI}$ . The SM assimilation  
486 improved more in humid regions, while the  $ubRMSD$  of  $ET_{SM}$  was slightly higher in South America. In  
487 the original LPJ-DGVM simulation, the sites with a negative bias were mostly located in the humid and  
488 dry-sub humid regions, while most of the sites in arid and semi-arid regions had underestimation (Fig.  
489 5-BIAS(a), Table S3). The assimilation improved ET at some of the overestimated sites, but the

490     underestimation over these sites showed little improvement.

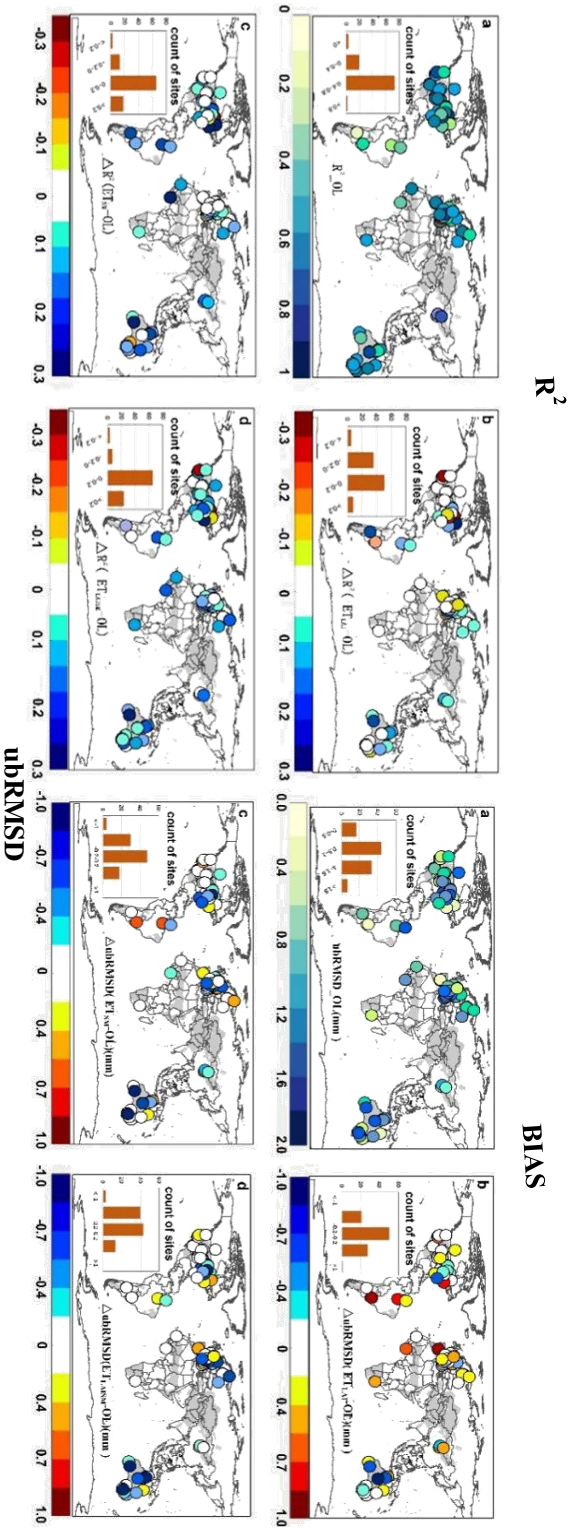


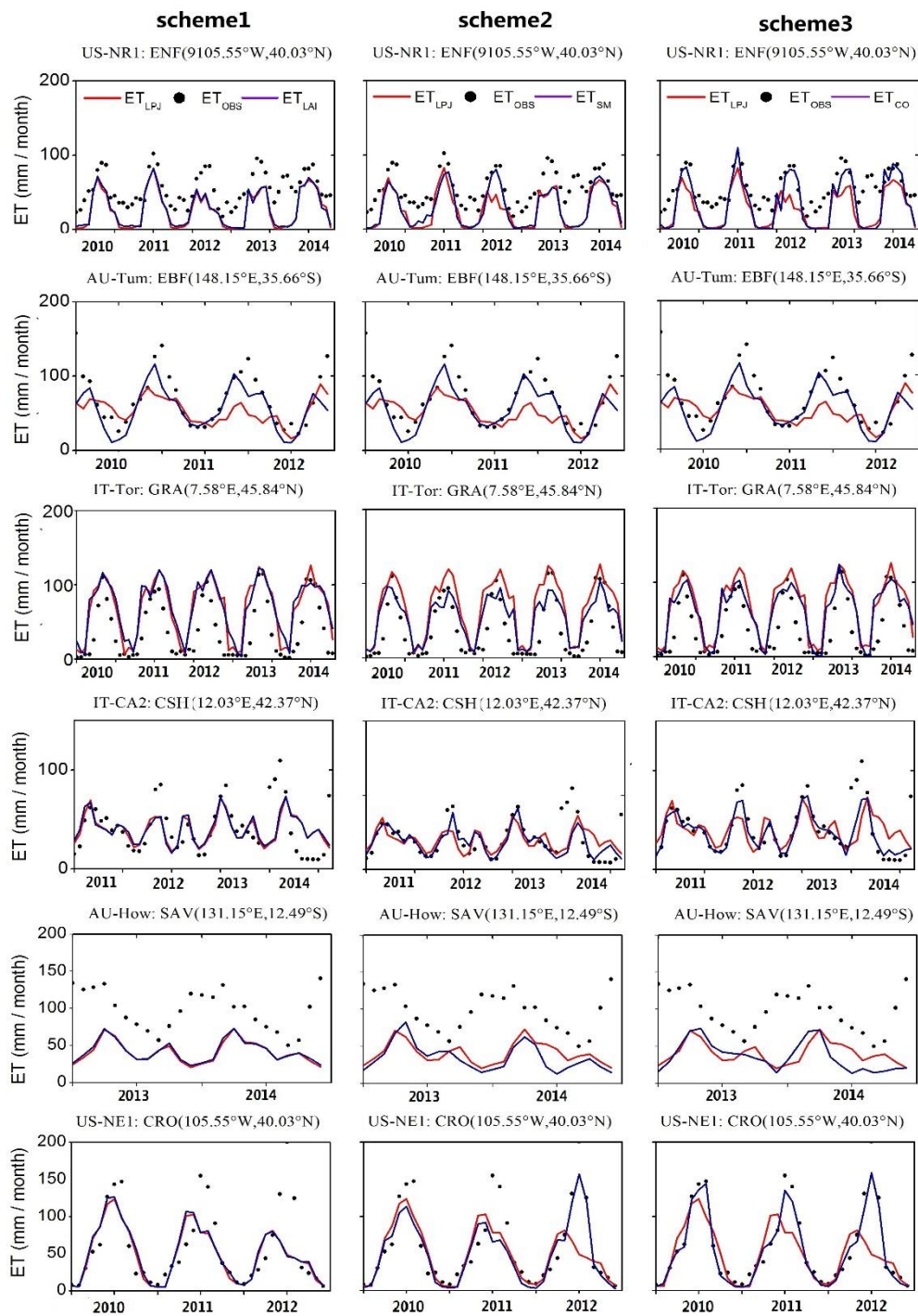
**Figure 5 (a)** The correlation coefficient, BIAS and the Unbiased Root Mean Square Error (ubRMSE) between the ET(GPP<sub>LPJ</sub>) simulated by the LPJ-DGVM and the site observations, with yellow/high correlation or ubRMSE; (b)  $\Delta R^2$  (correlation difference between ET<sub>SM</sub> and ET<sub>LPJ</sub>), BIAS (ET<sub>SM</sub>) and  $\Delta$ ubRMSE (ET<sub>SM</sub>-ET<sub>LPJ</sub>); (c)  $\Delta R^2$  (correlation difference between ET<sub>CO</sub> and ET<sub>LPJ</sub>), BIAS (ET<sub>CO</sub>) and  $\Delta$ ubRMSE (ET<sub>CO</sub>-ET<sub>LPJ</sub>), blue/red represent positive/negative value.

492 At the seasonal scale, the model simulations were able to capture the temporal trend of  $ET_{OBS}$ , and  
493 joint assimilation significantly improved the simulation in the growing season (US-NR1, US-NE1);  
494 overall underestimation was observed for  $ET_{OBS}$ , especially in winter (Figure 6). Overall, the linear fitting  
495 of monthly  $ET_{CO}$  and  $ET_{OBS}$  was closer to 1:1 than that of  $ET_{LAI}$  and  $ET_{SM}$  (Figure S6). The simulation  
496 accuracy of joint assimilation was better than that of separate assimilation, and the performance of the  
497 SM assimilation was better than that of the LAI assimilation.

498 The ET residual analysis (Figure S7 (right)) indicated that the three assimilation scheme errors  
499 showed underestimation for  $ET_{OBS}$ . In general, the error distribution of separate assimilations was more  
500 dispersed than that of the joint assimilation. Similar to the assimilation performance of GPP,  $ET_{CO}$  and  
501  $ET_{SM}$  significantly improved the overestimation of  $ET_{OBS}$ , but did not significantly improve the  
502 underestimation. For the  $ET_{CO}$ , most of the errors were distributed around -30–18 mm month<sup>-1</sup>. The region  
503 with high  $ET_{OBS}$  was considerably underestimated, and the maximum negative error reached -57 mm  
504 month<sup>-1</sup>.

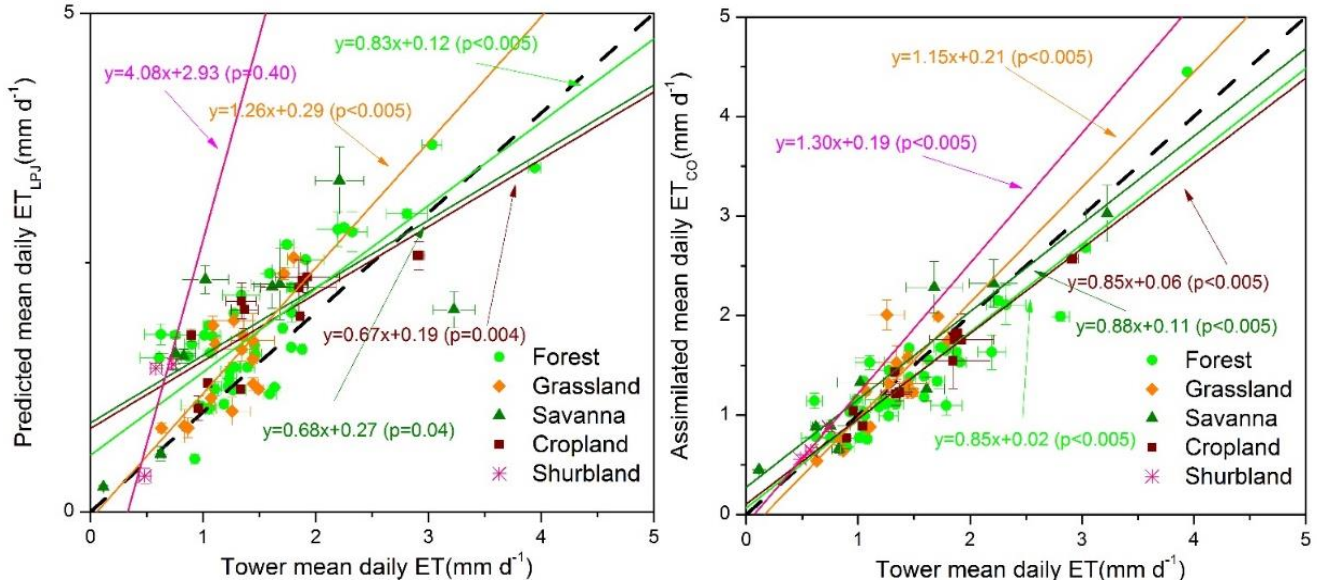
505 We also evaluated the ET assimilation results at the PFT scale (Figure 7). The results showed that  
506 our assimilated ET performed better at the site level ( $R^2= 0.77$ , ubRMSD= 0.65 mm d<sup>-1</sup>) than that of  
507  $ET_{LPJ}$  ( $R^2= 0.67$ , ubRMSD=0.95 mm d<sup>-1</sup>). Joint assimilation significantly reduced the errors of those  
508 shrubland sites with overestimation for  $ET_{OBS}$ , and the site distribution was closer to the 1:1 line. Our  
509 assimilation methods had better performance in forest, savanna, and grassland ecosystems than in  
510 cropland and shrubland (Table S3). The linear fitting results of grassland and shrubland were all above  
511 the 1:1 line, showing overall overestimation. Although the original simulation and assimilation  
512 performance were superior at savanna sites ( $R^2= 0.95$ , ubRMSD= 0.78 mm d<sup>-1</sup>), the standard deviations

513 of  $ET_{CO}$  and  $ET_{OBS}$  at savanna sites were relatively large, which was similar to the GPP results at savanna  
514 sites.





516 **Figure 6. Seasonal cycles of tower-based and simulated ET from Lund-Potsdam-Jena (LPJ), GLASS LAI**  
 517 **assimilation (scheme 1), SMOS assimilation (scheme 2) and joint assimilation (scheme 3) for the six sites**  
 518 **representing six PFTs during the study period.**



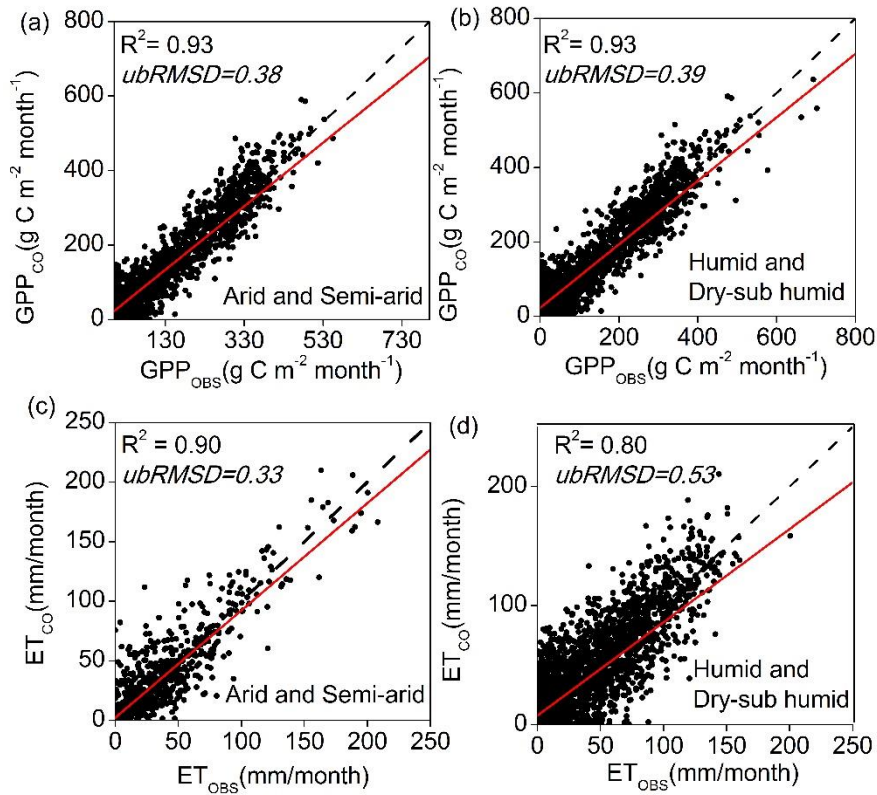
519

520

**Figure 7. Scatter plots of daily ET<sub>CO</sub> versus tower ET under different PFTs.**

521 *4.2. Comparison of assimilation performance in semi-arid and arid regions with that in humid and dry-*  
 522 *sub humid regions*





523

524 **Figure 8. Scatter plots of daily tower GPP and ET versus  $GPP_{CO}$  and  $ET_{CO}$  under arid and humid sites: (a)**  
 525 **and (c) are the fitting results of GPP and ET in arid and semi-arid regions, respectively; (b) and (d) are the**  
 526 **fitting results of GPP and ET in humid and dry sub-humid zone, respectively.**

527

528

529

530

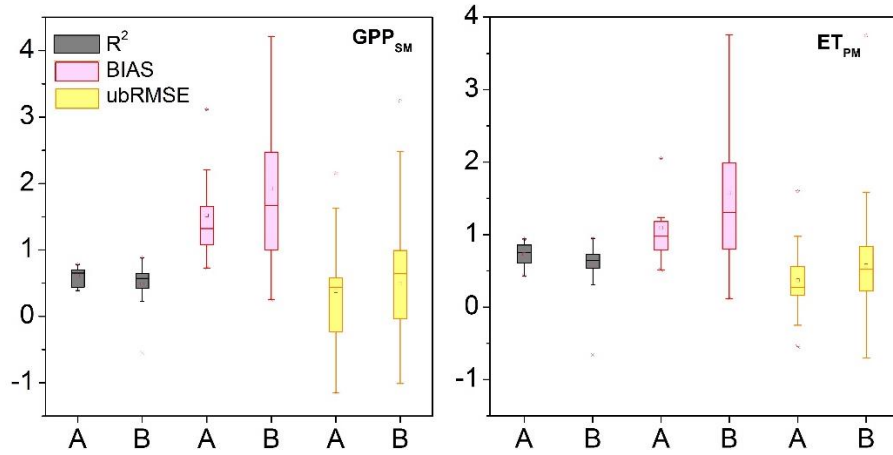
531

During the period 2010–2014, monthly  $GPP_{CO}$  and  $ET_{CO}$  performed differently in humid and sub-dry humid regions and semi-arid and arid regions (Figure 8, Table S2,3). Overall, the GPP and ET simulations had good consistency with the tower data in the two regions. For  $GPP_{CO}$ , there was no significant difference in the correlation and fitting coefficients between the two regions. As for  $ET_{CO}$ , the fitting results and  $R^2$  values in the semi-arid and arid regions performed better than those in the

532 humid and sub-dry humid regions, which also suggested the importance of surface SM for ET  
533 estimation in water-limited areas.

534 On the daily scale, the original GPP simulations ( $GPP_{LPJ}$ ) performed better in the semi-arid and  
535 arid regions than in the humid and sub-dry humid regions with higher  $R^2$  and lower ubRMSD (Table S2).  
536 the  $R^2$  and bias implied that the LAI assimilation alone had a better performance than the SM assimilation  
537 alone. However, for sites in arid and semi-arid areas, the RMSD and ubRMSD showed that the  $GPP_{SM}$   
538 improved better than  $GPP_{LAI}$ , which both demonstrated SM data are essential in water-limited regions.  
539 For  $GPP_{CO}$ , the shrubland in the semi-arid and arid regions had the lowest  $R^2$  values and the second lowest  
540 ubRMSD. The forest in the semi-arid and arid regions had the largest improvement after assimilation. In  
541 the humid and sub-dry humid regions, the  $GPP_{CO}$  of the savanna and cropland showed the largest  
542 improvement ( $R^2$  increased by 64.7% and 71.1%, respectively; ubRMSD decreased by 47.0% and 31.8%,  
543 respectively). The grassland in the semi-arid and arid regions had the highest  $R^2$ , and the savanna by  
544 combining all indicators had the best assimilation results compared to other types in both regions.

545 Similar to  $ET_{CO}$ , the  $ET_{LPJ}$  in the semi-arid and arid regions was better than that in humid and sub-  
546 dry humid regions in terms of four evaluation indicators (ubRMSD decreased by 34.4% in semi-arid and  
547 arid regions and the ubRMSD decreased by 30.9% in humid and sub-dry humid regions compared with  
548  $ET_{LPJ}$ ). The  $R^2$  and ubRMSD implied that the SM assimilation alone had a better performance than the  
549 LAI assimilation alone, especially for sites in arid areas. and the bias showed that the  $ET_{LAI}$  improved  
550 better than  $ET_{SM}$  for sites in humid and sub-dry humid areas. The performance of the original simulation  
551 and assimilation of grassland sites in the semi-arid and arid regions was the best among all five PFTs.

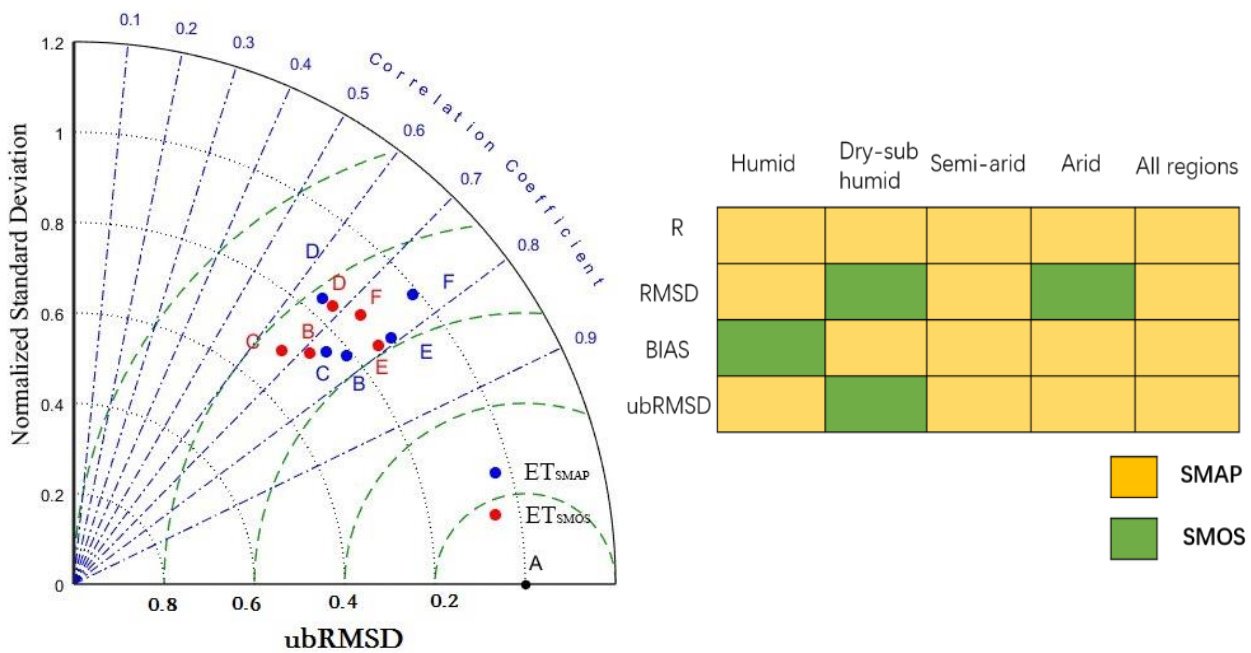


553

554 **Figure 9. Boxplots of  $R^2$ , ubRMSD and BIAS for  $GPP_{SM}$  (left) and  $ET_{PM}$  (right). A represents the sites in arid**  
 555 **and semi-arid areas, and B represents the sites in humid and dry sub-humid areas.**

556 To investigate the reasons for better assimilation performance in water-limited regions, we evaluated  
 557 the GPP and ET simulated by the LPJ-PM according to  $R^2$ , ubRMSD, and BIAS (Figure 7). Compared  
 558 with the semi-arid and arid regions, the humid and sub-dry humid region had smaller  $R^2$  mean, larger  
 559 BIAS, and no significant difference in mean ubRMSD for  $GPP_{SM}$ . In general, the evaluation results of  
 560 joint assimilation for  $ET_{PM}$  were generally consistent with those for  $GPP_{SM}$  and  $GPP_{SM}$ .  $ET_{PM}$  showed  
 561 underestimation, which was consistent with the underestimation in SM assimilation. These results  
 562 indicated that, both GPP and ET modeled by LPJ-PM with joint assimilation were less stable and had a  
 563 lower performance in the humid and sub-dry regions than in the semi-arid and arid regions.

564 *4.3. Comparison of assimilation performance in assimilating SMOS and SMAP soil moisture data*



A:Reference point B: Cropland C: Shrubland D: Forest E: Grassland F: Savanna

565

566

567

568

569

570

571

572

573

574

575

**Figure 10. Taylor diagram (left) comparing ET simulations with observations at all 46 AmeriFlux sites at the daily time step between April 2015 and December 2018. Blue dots represent results based on assimilation with SMAP SM only and red dots represent results based on assimilation with SMOS SM only. Reference points A and B-F correspond to the vegetation functional types (PFTs). The grid diagram (right) compares the evaluation indices of ET simulations with those of the observed values at all 46 AmeriFlux sites with different wet and dry zones at the daily time step; the yellow cells indicate that  $ET_{SMAP}$  performs better in the metric, and green cells indicate that  $ET_{SMOS}$  performs better in the metric. The Taylor chart was used to compare the assimilation performance of  $ET_{SMAP}$  and  $ET_{SMOS}$  at 46 AmeriFlux sites (Figure 10-left). The results showed that  $ET_{SMAP}$  performed better than  $ET_{SMOS}$  for all PFTs. Both  $ET_{SMAP}$  and  $ET_{SMOS}$  performed well for grassland (closer to point A), and there was little difference between  $R^2$  and**

576 standardized RMSD. The NSD of  $ET_{SMAP}$  in grassland was 0.88, which was closer to 1 than that of  $ET_{SMOS}$ .  
577 The assimilation of ET in the forest had a lower R and higher standardized RMSD (0.7-0.8) than those of  
578 other PFTs, and the NSD of cropland and shrubland was lower than that of other PFTs (0.6-0.8), indicating  
579 that the assimilation for cropland and shrubland could not reproduce the variations in ET effectively.  
580 However,  $ET_{SMAP}$  showed significant improvement in R compared with  $ET_{SMOS}$  for shrubland and  
581 cropland. The assimilation performance of  $ET_{SMAP}$  and  $ET_{SMOS}$  for savanna showed the greatest difference.  
582 In general, the  $ET_{SMAP}$  and  $ET_{SMOS}$  were slightly different, and the  $ET_{SMAP}$  was more improved than  
583  $ET_{SMOS}$ .

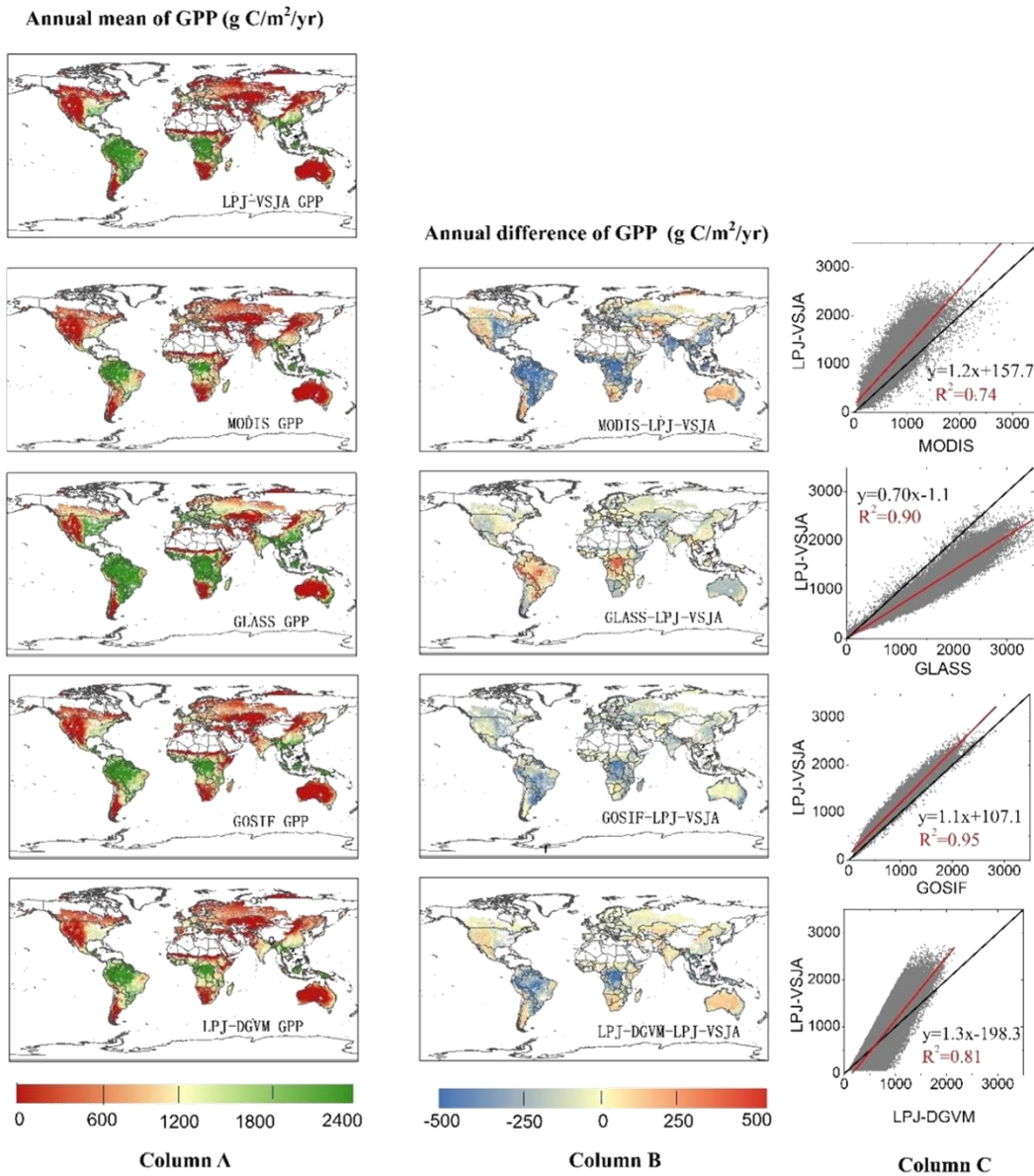
584 Figure 10 (right) shows the assimilation accuracy of  $ET_{SMOS}$  and  $ET_{SMAP}$  in different humid and arid  
585 regions. The  $ET_{SMAP}$  had significant advantages for the four indicators. The R of  $ET_{SMAP}$  was higher than  
586 that of  $ET_{SMOS}$  in all the areas. However,  $ET_{SMOS}$  in some evaluation indicators showed a better  
587 performance than  $ET_{SMAP}$  (BIAS in the humid region; ubRMSD in the sub-dry humid region). This may  
588 be due to the overall more humid nature of SMOS SM than the SMAP SM. Moreover, the sensitivity of  
589 deep soil moisture contributed more to the ET in humid areas than in the water-limited areas.

#### 590 *4.4. Global simulations of GPP and ET with joint assimilation of LAI and soil moisture data*

591 To assess the spatial scalability of the LPJ-VSJA assimilation scheme, we simulated the global daily  
592 GPP and ET for 2010–2018 with a spatial resolution of  $0.25^\circ$ . The original results simulated by the LPJ-  
593 DGVM and LPJ-VSJA were referred to as LPJ-DGVM GPP(ET) and LPJ-VSJA GPP(ET), respectively.  
594 We compared the annual spatial GPP and ET values and the error standard deviation of the LPJ-VSJA  
595 with several existing flux products.

596            Figures 11 and 12 depict the spatial distribution of the annual mean and the differences between our  
597 simulation results and the global independent satellite-based products. The developed LPJ-VSJA GPP  
598 was the closest to GOSIF GPP (Li and Xiao 2019) in most regions with the lowest spatial mean deviation  
599 (LPJ-VSJA-GOSIF) ( $27.9 \text{ g C m}^{-2} \text{ yr}^{-1}$ ), followed by GLASS GPP ( $51.2 \text{ g C m}^{-2} \text{ yr}^{-1}$ ) (Yuan et al. 2010),  
600 LPJ-DGVM ( $-73.4 \text{ g C m}^{-2} \text{ yr}^{-1}$ ), and MODIS GPP ( $93.1 \text{ g C m}^{-2} \text{ yr}^{-1}$ ). LPJ-VSJA had higher GPP values  
601 than GOSIF GPP in tropical regions, such as Amazonia, Central Africa, and Southeast Asia. In general,  
602 the annual mean and differences between MODIS, GOSIF GPP, LPJ-DGVM, and our LPJ-VSJA were  
603 in broad agreement (with higher  $R^2$  ranging from 0.74 to 0.95).

604            LPJ-VSJA ET was the closest to GLEAM ET on the spatial average with the least spatial average  
605 deviation ( $-13.9 \text{ mm yr}^{-1}$ ) and highest  $R^2$  (0.88), followed by GLASS ET ( $-23.1 \text{ mm yr}^{-1}$  and 0.82), GLDAS  
606 ET ( $-34.7 \text{ mm yr}^{-1}$  and 0.73), LPJ-DGVM ( $-48.7$  and  $0.66 \text{ mm yr}^{-1}$ ), and MODIS ET ( $-122.1$  and  $0.54 \text{ mm}$   
607  $\text{yr}^{-1}$ ).

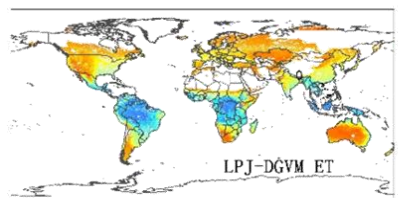
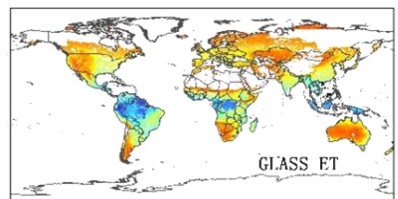
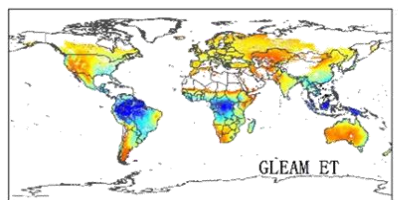
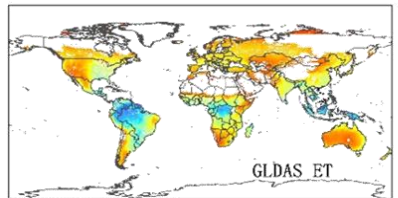
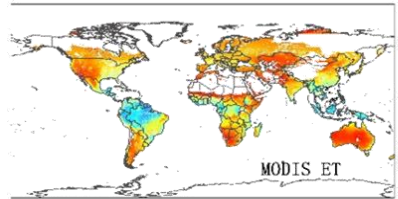
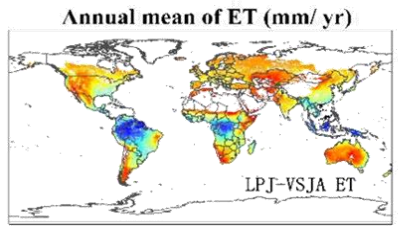


608

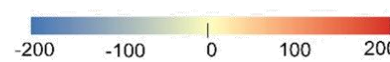
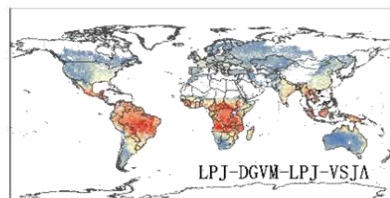
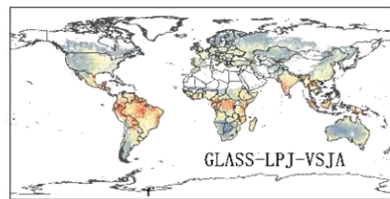
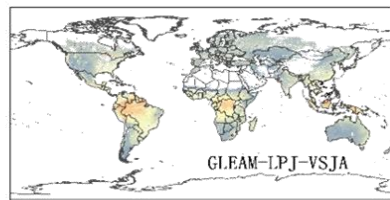
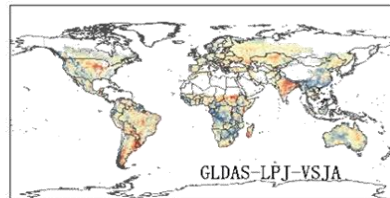
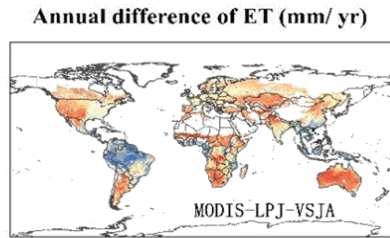
609 **Figure 11. Column A: Spatial distribution of annual LPJ-VSJA GPP and other independent satellite-based**  
 610 **datasets (a: MODIS GPP; b: GLASS GPP; c: GOSIF GPP; e: LPJ-DGVM). Column B: Spatial**  
 611 **distribution of the difference between annual LPJ-VSJA GPP and other independent satellite-based**

612 **datasets. Column C: Scatter plots between these products. Black lines show the 1:1-line, red lines show the**  
613 **regression fit.**

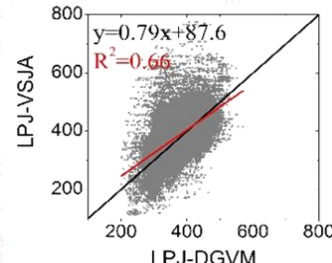
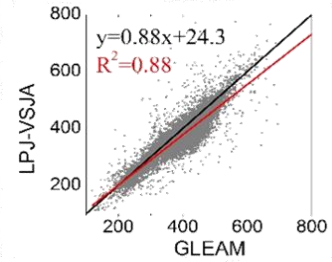
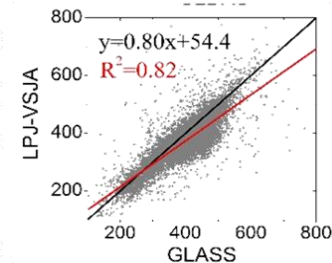
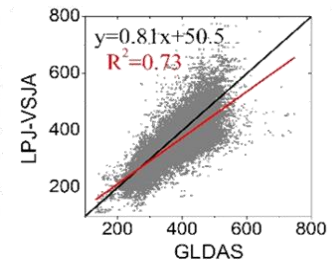
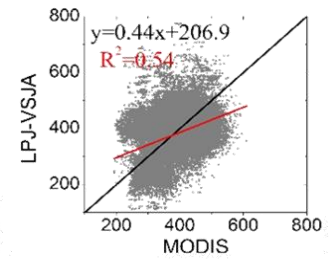




**Column A**



**Column B**



**Column C**

615 **Figure 12. Column A: Spatial distribution of annual LPJ-VSJA ET and other independent satellite-**  
616 **based datasets (a: MODIS GPP; b: GLDAS ET; c: GLEAM ET; d: GLASS ET; e: LPJ-DGVM ET).**  
617 **Column B: Spatial distribution of the difference between annual LPJ-VSJA ET and other independent**  
618 **satellite-based datasets. Column C: Scatter plots between these products are provided on the right of the**  
619 **difference maps. Black lines show the 1:1-line, red lines show the regression fit.**  
620

621 Figure 13 (a)–(e) represent the spatial error standard deviation ( $\sigma$ ) distribution of MODIS, GLASS,  
622 GOSIF, and LPJ-VSJA GPP, respectively. The graphs on the right side depict the corresponding  
623 histograms. The  $\sigma$  of the MODIS GPP was evenly distributed between 30 and 60 g C m<sup>-2</sup> month<sup>-1</sup>, while  
624 the average  $\sigma$  of other products was concentrated in 0–20 g C m<sup>-2</sup> month<sup>-1</sup> (90%). The high errors of all  
625 products were concentrated in the high temperature and humid areas of southern North America, eastern  
626 South America, humid and dry sub-humid areas of South Asia, and the savannas of Africa and Australia.  
627 The error histogram of GOSIF GPP and LPJ-DGVM GPP were in line with the normal distribution, with  
628 an average value of 8.3 g C m<sup>-2</sup> month<sup>-1</sup> and 22.4 g C m<sup>-2</sup> month<sup>-1</sup>. The GLASS GPP product had the  
629 lowest mean value (3.6 g C m<sup>-2</sup> month<sup>-1</sup>), followed by LPJ-VSJA (4.7 g C m<sup>-2</sup> month<sup>-1</sup>), but the error  
630 variance of the LPJ-VSJA product was the lowest, indicating a stability of the regional error (Table S4).  
631 Compared to the LPJ-DGVM, the joint assimilation results showed improvement in all regions (the  
632 average error reduced by 17.7 g C m<sup>-2</sup> month<sup>-1</sup>), especially in the humid regions of South Asia, Australia,  
633 and the United States. Our LPJ-VSJA GPP was generally proven to have high accuracy and stability for  
634 spatial analysis and could provide a reference for other model products.

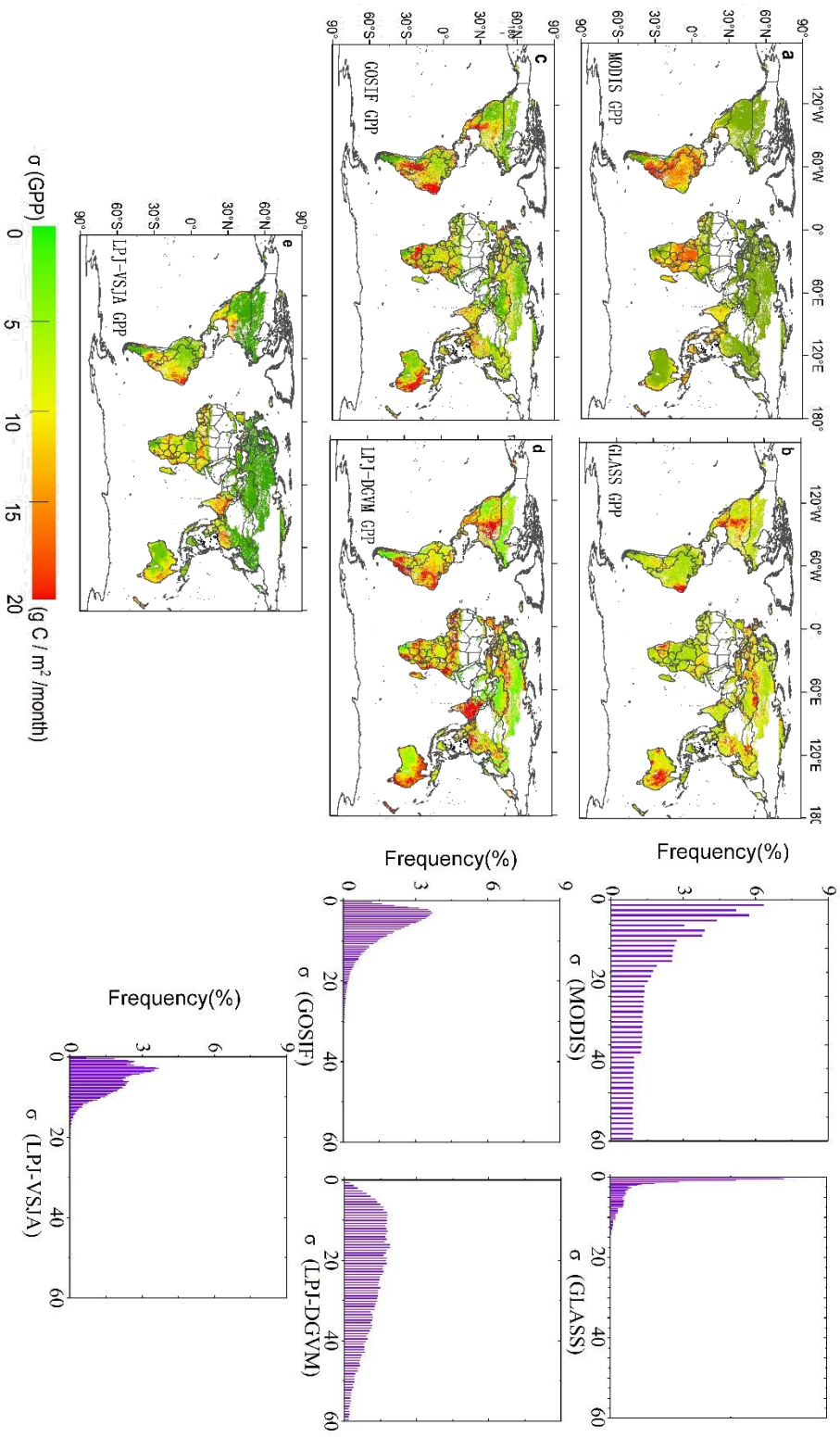


**Figure 13. Spatial distribution and histograms of error standard deviation ( $\sigma$ ) for global GPP products: MODIS (a), GOSIF (b), GLASS (c), LPJ-DGVM (d), and LPJ-VSJA (e).**

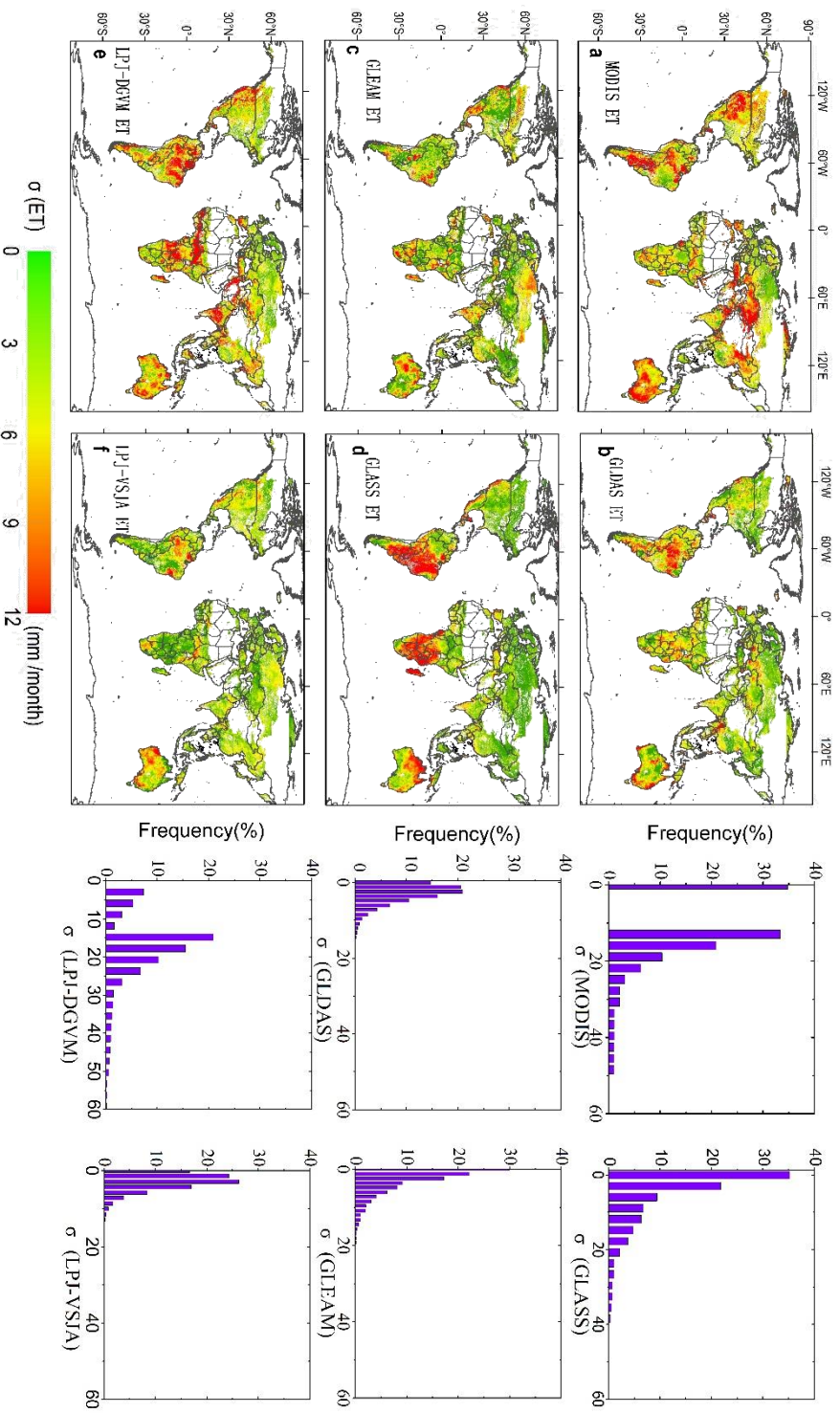


Figure 4. Spatial distribution and histograms of error standard deviation ( $\sigma$ ) for global ET products:

MODIS (a),GLDAS (b),GLEAM (c), GLASS (d), LPJ-DGVM (e), and LPJ-VSJA (f).

637 Figures 14 (a)–(f) show the  $\sigma$  of MODIS, GLDAS, GLEAM, GLASS, and LPJ-VSJA ET (the units  
638 are mm/month), and the right graphs are the corresponding histograms. The  $\sigma$  values of GLDAS and LPJ-  
639 VSJA represented a normal distribution trend. Except for MODIS, GLASS, and LPJ-DGVM (0–60 mm  
640 month<sup>-1</sup>), the  $\sigma$  of other products was generally between 0-20 mm month<sup>-1</sup>. The simulation error was  
641 relatively smaller in the Northern Hemisphere than in the Southern Hemisphere, especially for GLASS  
642 ET and GLDAS ET. Significant improvements in joint assimilation were observed in the northern  
643 hemisphere (especially in the semi-arid areas of the western United States and savanna and cropland areas  
644 of central India) and African savanna areas, and the average error was reduced by 15.1 mm month<sup>-1</sup>. In  
645 general, the error mean and variance of LPJ-VSJA and GLEAM products were relatively low (Table S4),  
646 and there was no apparent extremely high value region in the error distribution. Among the five products,  
647 LPJ-VSJA had the lowest error mean and variance and the highest accuracy.

## 648 **5. Discussion**

### 649 *5.1 Advantage of joint assimilation for GPP and ET*

650 The benefit of employing multiple data flows in an assimilation system is the complementarity of  
651 the data, which enables constraints on different components of the underlying process-based terrestrial  
652 biosphere model. Due to the interaction and feedback between the internal components of the model, the  
653 assimilation of multiple observations has a synergistic effect, and the integrated constraints are greater  
654 than the individual constraint (Kato et al. (2013)). The advantage of our joint assimilation is that it can  
655 improve the simulation accuracy of both GPP and ET, especially ET, in arid and semi-arid regions.

656 In the GPP assimilation experiment, the performance of the LAI assimilation was better than that of  
657 the SSM assimilation possibly for two reasons: (1) the LPJ-VSJA is more controlled by LAI data because  
658 the ratio of assimilated LAI (daily input) to SSM observations (3-day interval input) is approximately 3:1,  
659 which makes the likelihood function biased to LAI data; (2) the SM directly influences the simulation of  
660 ET, and the corresponding time function (computes the top layer SM (50 cm)) used here by Zhao et al.  
661 (2013) will result in the error of the updated top SM and propagating the error to the  $GPP_{SM}$ . In addition,  
662 the 8-day interval LAI has the capability to capture the temporal variability of phenology.

663 Current studies on terrestrial water and carbon flux assimilation mostly focus on the assimilation  
664 between a single model framework and observation results, lacking the fusion and comparison between  
665 multiple models. The processed models used in DA are simplifications and approximations of reality, and  
666 different models focus on different ecological processes. In this study, the updated ET module was

667 integrated to compensate for the simplification of soil stratification and the lack of SM information in the  
668 hydrological module of the LPJ-DGVM. Therefore, the integration of multiple types of models and multi-  
669 source observation data (remotely sensed data, ecological inventory data (National Ecological  
670 Observatory Network, NEON (Keller et al. 2008)), and other measurements (Desai et al. 2011; Hayes et  
671 al. 2012) is expected to more objectively and effectively simulate the real state of ecosystems.

## 672 *5.2 Comparison of joint assimilation (LPJ-VSJA) and other models for GPP and ET across regions and* 673 *vegetation types*

674 Global GPP and ET for different products were calculated by multiplying the global mean GPP  
675 density flux with the global vegetation area (122.4 million km<sup>2</sup>) originated from the MODIS land cover  
676 product (Friedl et al. 2010). The mean global GPP of the LPJ-VSJA (130.2 Pg C yr<sup>-1</sup>) was  
677 approximately 12% lower than that of PML-V2 (145.8 Pg C yr<sup>-1</sup>) and 18% higher than that of GLASS  
678 and MODIS, respectively (Table S6). The GPP values of LPJ-VSJA and GOSIF were the most similar.  
679 The GOSIF GPP was developed from gridded SIF using simple linear relationships between SIF and  
680 GPP. Our global LPJ-VSJA GPP estimates were within the currently most plausible 110–150 Pg C/yr  
681 range.

682 As for ET, our results were similar to those of GLEAM ET and lower than those of PML-V2,  
683 GLDAS-2, and GLASS ET (~72000 mm yr<sup>-1</sup>). Joint assimilation improved the overestimation of LPJ-  
684 DGVM ET. At the daily scale, the estimation accuracy of PML-V2 and GLDAS-2 products, calibrated  
685 with flux tower data, was better than that of our estimates, which suggests an underestimation of LPJ-

686 VSJA ET in wet regions. It is likely because the SM of SMAP or SMOS was underestimated in the wet  
687 region or the influence of deep SM was under-represented. According to Seneviratne et al. (2010),  
688 satellite-based ET estimation approaches often overestimate ET in areas of arid and semi-arid climatic  
689 regimes in the magnitude of 0.50 to 3.00 mm d<sup>-1</sup>. The poor performance of these models can largely be  
690 attributed to the lack of constraints of SM and more accurate vegetation parameters (Gokmen et al. 2012;  
691 Pardo et al. 2014). For instance, the monthly estimated ET modeled by the Penman-Monteith-Leuning  
692 (PML) model agreed with flux tower data well ( $R^2 = 0.77$ ; bias = - 9.7%, approximately 0.2 mm d<sup>-1</sup>).  
693 Our annual ET simulations were lower than other products and slightly underestimated tower ET with a  
694 bias of 0.19 mm d<sup>-1</sup> ( $ET_{OBS} - ET_{CO}$ ).

695 In general, GPP and ET had better assimilation performance in arid and semi-arid regions than in  
696 humid and semi-humid regions likely because of the following reasons. First, the incorporation of surface  
697 SM is more important for vegetation growth in water-limited areas. The module PT-JPL<sub>SM</sub> has been  
698 proven to have better performance in semi-arid and arid regions (Purdy et al. 2018). Our integrated model  
699 LPJ-PM also performed better in semi-arid and arid regions by assimilating SMAP soil moisture (Li et al.  
700 2020). Second, the input performance, including SMOS and SMAP SM products, is better in arid and  
701 temperate regions than in cold and humid regions (Zhang et al. 2019). Third, the vegetation types in humid  
702 regions are more complex and relatively less accurately simulated by the LPJ-DGVM within a single grid  
703 cell. For comparison, Zhang et al. (2020) used a data-driven upscaling approach to estimate GPP and ET  
704 in global semi-arid regions. This data-driven approach ( $R^2 = 0.79$ , RMSD = 1.13 g C m<sup>-2</sup> d<sup>-1</sup>) had slightly  
705 higher performance in estimating GPP than our LPJ-VSJA ( $R^2 = 0.73$  and RMSD = 1.14 g C m<sup>-2</sup> d<sup>-1</sup>) and



706 the data-driven method ( $R^2 = 0.72$  and  $\text{RMSD} = 0.72\text{mm d}^{-1}$ ) had identical performance for estimating  
707 ET with our LPJ-VSJA ( $R^2 = 0.73$  and  $\text{RMSD} = 0.72\text{ mm d}^{-1}$ ).

708 Our assimilation performance varied with PFT. The GPP and ET assimilation results of savanna sites  
709 performed well in both dry and wet regions, and those of shrubland sites showed the most remarkable  
710 improvement for simulations of LPJ-DGVM. The original simulation and assimilation performance of  
711 grassland sites in the semi-arid and arid regions were the best for all five PFTs. Consistent with our  
712 research, previous studies also showed better GPP or ET simulations for grassland, savannas, and  
713 shrublands biomes. For instance, Feng et al. (2015) validated five satellite-based ET algorithms for semi-  
714 arid ecosystems and concluded that all the models produced acceptable and relatively better results for  
715 most grassland, savanna, and shrubland sites. Yang et al. (2017) demonstrated that the GLEAM ET had a  
716 superior performance for the grassland sites. The GOSIF GPP demonstrated better simulation for  
717 grassland and woody savannas sites at 8-day time steps with higher  $R^2$  (0.77 and 0.83, respectively) and  
718 lower RMSD ( $1.48\text{ g C m}^{-2}\text{ d}^{-1}$  and  $1.1\text{ g C m}^{-2}\text{ d}^{-1}$ ) (Li and Xiao 2019). In contrast, our LPJ-VSJA GPP  
719 showed an  $R^2$  of 0.87 for grassland and 0.75 for savannas and an RMSD of  $1.11\text{ g C m}^{-2}\text{ d}^{-1}$  and  $1.1\text{ g C}$   
720  $\text{m}^{-2}\text{ d}^{-1}$ , respectively, in semi-arid and arid regions.

### 721 *5.3 Uncertainty analysis of joint assimilation*

722 Our validation results at both site and regional scales indicated that uncertainty existed in LPJ-VSJA  
723 daily GPP and ET estimates. The errors from the tower EC observations, model-driven data, model  
724 structure, error of satellite-based observations (e.g., LAI and SM), and the spatial scale mismatch between

725 the ground observed footprint size and satellite-derived footprint size were the vital factors affecting  
726 assimilation performance.

727 First, recent studies have revealed errors in the GLASS LAI and SMOS or SMAP SM compared  
728 with ground measurements. By computing the RMSD and  $R^2$  of each product, the GLASS LAI accuracy  
729 was clearly superior to that of MODIS and Four-Scale Geometric Optical Model based LAI (FSGOM) in  
730 forests and GLASS and FSGOM led to in much higher annual GPP and ET estimates compared to  
731 MCD15(Liu et al. 2018). The vegetation type (or land cover) misclassification caused 15–50% differences  
732 in LAI retrieval (Fang and Liang 2005; Gonsamo and Chen 2011). Yan et al. (2016) calculated a RMSD  
733 of 0.18 for the GLASS LAI over a range of HeiHe drainage basin sites and used the error to improve the  
734 simulation of LAI and fluxes by assimilating GLASS LAI data. Previous studies reported an improvement  
735 in the performance of the SMOS and SMAP products (Lievens et al. 2015; Miernecki et al. 2014), which  
736 both provide an accuracy of  $0.04 \text{ m}^3 \text{ m}^{-3}$  (Zhang et al. 2019). However, the actual observation error of  
737 these two products typically depends on the spatial location and time of the year (RMSD varying between  
738  $0.035$  and  $0.056 \text{ m}^3 \text{ m}^{-3}$  for several retrieval configurations) (Brocca et al. 2012). According to Purdy et  
739 al. (2018), the ET simulated by PT-JPL<sub>SM</sub> using the 9 km SM\_L3\_P\_E data showed an inferior agreement  
740 ( $R^2= 0.47$ ) but a relatively low RMSD ( $0.77 \text{ mm d}^{-1}$ ), due to the SMAP errors in the grid cell with soil  
741 heterogeneity and the climatological differences between model SM forecasts and SMAP SM (Reichle  
742 and Koster 2004). We rescaled the  $ET_{PM}$  to the probability distribution of the  $ET_{LPJ}$  through a cumulative  
743 distribution function (CDF) to correct the potential seasonal biases of  $ET_{PM}$  before assimilation.

744 Second, there is large uncertainty in the influence of root zone SM as the source of water available  
745 to plants (Albergel et al. 2008; Bonan et al. 2020). Our GPP results of cropland sites were largely  
746 influenced by US-Ne1, an irrigate site. This site maintained high annual GPP in 2012 despite the drought  
747 (Figure S4). However, the SMOS SM in 2012 had a lower surface SM annual mean than the site  
748 observations likely because the detected soil layer (0-50 cm) of the site observation is deeper than that of  
749 the satellite retrieval and the cumulative deep soil moisture due to the regular irrigation was higher than  
750 the surface SM that could easily be vaporized during the drought period (Figure S4). Therefore, the  
751 influence of deep SM of some cropland sites during the drought years induced large simulation errors and  
752 unsatisfactory assimilation performance. Moreover, some deep-rooted forests maintain a high LAI during  
753 drought by absorbing deep SM (>2 m) and groundwater (Zhang et al. 2016). Thus, joint assimilation of  
754 the LAI and SM may eliminate a portion of the underestimation of GPP of such vegetation in drought  
755 periods. Therefore, further research is needed on how to optimally utilize satellite SM data for improving  
756 GPP and ET simulations.

757 Third, the problem of mixed pixels and mismatches in the observation footprints may also have an  
758 influence on the accuracy of estimated GPP and ET. The 5 km spatial resolution of the GLASS LAI ,9  
759 km of SMAP, and 25 km of SMOS products cannot capture the sub-grid-scale condition, especially in  
760 grid cells for complex land surfaces or strong soil heterogeneity. To ensure the consistency of the grid-  
761 cell representativeness for the LAI and SM, the interpolation result in errors that propagate through the  
762 modeling and assimilation, causing the accumulation of output errors (Nijssen and Lettenmaier 2004).  
763 Moreover, the shrubland in the LPJ-DGVM was most likely simulated as C4 grassland in the

764 hydrothermal condition of semi-arid and arid regions. In contrast, the shrubland tended to be hybrid  
765 vegetation types (grassland mixed with other types of forest vegetation) in the hydrothermal condition of  
766 humid and sub-dry humid regions, and the simulated canopy height is closer to the real condition of  
767 shrubland. This might also be the reason for the superior performance of  $ET_{LPJ}$  and assimilation results  
768 of shrubland sites in humid and sub-dry humid regions.

769       When assimilating multiple data streams, all data streams could be in the same optimization  
770 (simultaneous assimilation) or use a sequential (step-by-step) approach. Mathematically, simultaneous  
771 optimization is optimal because strong parametric connections are maintained between different  
772 processes. However, complications may arise due to computational constraints related to the inversion of  
773 large matrices or the requirement of numerous simulations, particularly for global datasets (e.g. Peylin et  
774 al.,2016), and due to the “weight” of different data streams in the optimization (e.g. Wutzler and  
775 Carvalhais, 2014). This is particularly true when considering a regional-to-global-scale, multiple site  
776 optimization of a complex model that contains many parameters, and which typically takes on the order  
777 of minutes to an hour to run a one-year simulation. In practice, it is very difficult to define a probability  
778 distribution that properly characterizes the model structural uncertainty and observation errors accounting  
779 for biases and non-Gaussian distributions. Nevertheless, a step-wise assimilation may be useful in dealing  
780 with possible inconsistencies on a temporary basis, since parameter error covariance matrix must be  
781 propagated at each step. It’s worth noting that the deviation between the model and observational data  
782 should be solved in the process of step-wise assimilation, such as the joint assimilation in this study, the  
783 satellite observations and model simulation were fitting through the CDF method so that the first step

784 assimilation will strongly constrain the uncertainty of parameters related to phenology and carbon flux  
785 and propagate to the second step . Alternative solutions were found for water -related parameters through  
786 soil moisture, providing a better fit for all data streams. The sequence of assimilation is essential in the  
787 step-wise assimilation, and if the first observation contains a strong bias, then the associated error  
788 correlation will also propagate through the first assimilation. If the autocorrelation in the observation error,  
789 or the correlation between the data stream errors is not considered, it is likely that the posterior simulation  
790 has been overturned. That is, we overestimate the reduction in parametric uncertainty. If two observational  
791 data are less uncertainty (i.e., high precision of observation data), and the model of deviation is smaller  
792 (depend on the spatial scale and inversion method). Moreover, the correlation of these observations is  
793 stronger, and contain enough spatio-temporal information to limit all the parameters optimization  
794 accurately, the step-wise assimilation performance is basically the same as that of simultaneous  
795 assimilation.

## 796 **6. Conclusions**

797 We developed an assimilation system LPJ-VSJA that integrates GLASS LAI, SMOS SM, and  
798 SMAP SM data to improve GPP and ET estimates globally. The system was designed to assimilate two  
799 SM products (SMOS and SMAP) into the integrated model - LPJ-PM for both dry and humid regions  
800 through separate and joint assimilation. The results show that the joint constraints provided by vegetation  
801 and soil variable strategies improve model simulations. Both the original and joint assimilation results for  
802 GPP and ET in semi-arid and arid regions performed better than those in humid and dry-sub humid regions,

803 and the LPJ-PM that emphasized the SM information is more suitable for the water-limited regions. For  
804 ET assimilation, the different SM products influence assimilation performance, and SMAP SM possesses  
805 a slight advantage in most vegetation types and in both dry and humid regions. Our global LPJ-VSJA  
806 GPP and ET products have relatively higher accuracy than other products, especially in water-limited  
807 regions with lower ET values.

### 808 **Data availability**

809 The LPJ-DGVM v4.1 version code (LPJ-ML) and example configurations are public available via the  
810 project homepage (<https://github.com/PIK-LPJmL/LPJmL>). We used the 3.01 version of LPJ-DGVM,  
811 which removed the agricultural management module. The access of all the input and validation dataset of  
812 assimilation system have been described in article. The assimilation method code configured by Fortran  
813 platform could be provided by contacting the X.T co-author. The modified code of LPJ-PM model and  
814 the underlying and global LPJ-VSJA GPP and ET data can be obtained by contacting the lead author of  
815 this manuscript.

### 816 **Author contributions**

817 S.L. and L.Z. designed the experiment and wrote the paper with support from all coauthors. S.L. and R.M.  
818 implemented the codes necessary for the experiments. J.X. contributed to the structure of the article and  
819 comparison of assimilation performance between the SMOS and SMAP experiments. X.T provided the  
820 POD-En4DVAR method and the code. M.Y contributed to the validation and analysis of the results. All  
821 the authors contributed to the synthesis of results and key conclusions.

822 **Competing interests**

823 The authors declare that they have no known competing financial interests or personal relationships that  
824 could have appeared to influence the work reported in this paper.

825

826 **Financial support**

827 S.L., L.Z., R.M., and M.Y. were funded by the National Natural Science Foundation of China (Grant No.  
828 41771392; PI Li Zhang) and (Grant No. 41901364; PI Min Yan).

829

830 **References**

- 831 Albergel, C., Rüdiger, C., Pellarin, T., Calvet, J.-C., Fritz, N., Froissard, F., Suquia, D., Petitpa, A., Pignatelli, B., & Martin,  
832 E. (2008). From near-surface to root-zone soil moisture using an exponential filter: an assessment of the method based  
833 on in-situ observations and model simulations. *Hydrology and Earth System Sciences*, 12, 1323-1337
- 834 Albergel, C., Calvet, J.-C., Mahfouf, J.-F., Rüdiger, C., Barbu, A. L., Lafont, S., Roujean, J.-L., Walker, J. P., Crapeau,  
835 M., and Wigneron, J.-P.: Monitoring of water and carbon fluxes using a land data assimilation system: a case study for  
836 southwestern France, *Hydrol. Earth Syst. Sci.*, 14, 1109–1124, <https://doi.org/10.5194/hess-14-1109-2010>, 2010.
- 837 Albergel, C., Zheng, Y., Bonan, B., Dutra, E., Rodríguez-Fernández, N., Munier, S., Draper, C., de Rosnay, P., Muñoz-  
838 Sabater, J., Balsamo, G., Fairbairn, D., Meurey, C., and Calvet, J.-C.: Data assimilation for continuous global assessment  
839 of severe conditions over terrestrial surfaces, *Hydrol. Earth Syst. Sci.*, 24, 4291–4316, [https://doi.org/10.5194/hess-24-](https://doi.org/10.5194/hess-24-4291-2020)  
840 [4291-2020](https://doi.org/10.5194/hess-24-4291-2020), 2020.
- 841 Anav, A., Friedlingstein, P., Beer, C., Ciais, P., Harper, A., Jones, C., Murray - Tortarolo, G., Papale, D., Parazoo, N.C.,  
842 & Peylin, P. (2015). Spatiotemporal patterns of terrestrial gross primary production: A review. *Reviews of Geophysics*,  
843 53, 785-818
- 844 Barth, A., Beckers, J.-M., Troupin, C., Alvera-Azcárate, A., & Vandenbulcke, L. (2014). divand-1.0: n-dimensional  
845 variational data analysis for ocean observations. *Geoscientific Model Development*, 7, 225-241
- 846 Blyverket, J., Hamer, P.D., Bertino, L., Albergel, C., Fairbairn, D., & Lahoz, W.A. (2019). An Evaluation of the EnKF  
847 vs. EnOI and the Assimilation of SMAP, SMOS and ESA CCI Soil Moisture Data over the Contiguous US. *Remote*  
848 *Sensing*, 11, 478

- 849 Bonan, B., Albergel, C., Zheng, Y., Barbu, A.L., Fairbairn, D., Munier, S., & Calvet, J.-C. (2020). An ensemble square  
850 root filter for the joint assimilation of surface soil moisture and leaf area index within the Land Data Assimilation System  
851 LDAS-Monde: application over the Euro-Mediterranean region. *Hydrology and Earth System Sciences*, 24, 325-347
- 852 Bonan, G., Williams, M., Fisher, R., & Oleson, K. (2014). Modeling stomatal conductance in the earth system: linking  
853 leaf water-use efficiency and water transport along the soil–plant–atmosphere continuum. *Geoscientific Model  
854 Development*, 7, 2193-2222
- 855 Brocca, L., Tullo, T., Melone, F., Moramarco, T., & Morbidelli, R. (2012). Catchment scale soil moisture spatial–  
856 temporal variability. *Journal of hydrology*, 422, 63-75
- 857 Burgin, M.S., Colliander, A., Njoku, E.G., Chan, S.K., Cabot, F., Kerr, Y.H., Bindlish, R., Jackson, T.J., Entekhabi, D.,  
858 & Yueh, S.H. (2017). A comparative study of the SMAP passive soil moisture product with existing satellite-based soil  
859 moisture products. *IEEE Transactions on Geoscience and Remote Sensing*, 55, 2959-2971
- 860 Caires, S., & Sterl, A. (2003). Validation of ocean wind and wave data using triple collocation. *Journal of geophysical  
861 research: oceans*, 108
- 862 Chan, S.K., Bindlish, R., O'Neill, P.E., Njoku, E., Jackson, T., Colliander, A., Chen, F., Burgin, M., Dunbar, S., &  
863 Piepmeier, J. (2016). Assessment of the SMAP passive soil moisture product. *IEEE Transactions on Geoscience and  
864 Remote Sensing*, 54, 4994-5007
- 865 Cui, C., Xu, J., Zeng, J., Chen, K.-S., Bai, X., Lu, H., Chen, Q., & Zhao, T. (2018). Soil moisture mapping from satellites:  
866 An intercomparison of SMAP, SMOS, FY3B, AMSR2, and ESA CCI over two dense network regions at different spatial  
867 scales. *Remote Sensing*, 10, 33
- 868 Desai, A.R., Moore, D.J., Ahue, W.K., Wilkes, P.T., De Wekker, S.F., Brooks, B.G., Campos, T.L., Stephens, B.B.,  
869 Monson, R.K., & Burns, S.P. (2011). Seasonal pattern of regional carbon balance in the central Rocky Mountains from  
870 surface and airborne measurements. *Journal of Geophysical Research: Biogeosciences*, 116
- 871 Draper, C., Mahfouf, J.-F., Calvet, J.-C., Martin, E., & Wagner, W. (2011). Assimilation of ASCAT near-surface soil  
872 moisture into the SIM hydrological model over France. *Hydrology and Earth System Sciences*, 15, 3829-3841
- 873 Entekhabi, D., Njoku, E.G., O'Neill, P.E., Kellogg, K.H., Crow, W.T., Edelstein, W.N., Entin, J.K., Goodman, S.D.,  
874 Jackson, T.J., & Johnson, J. (2010). The soil moisture active passive (SMAP) mission. *Proceedings of the IEEE*, 98,  
875 704-716
- 876 Etheridge, D.M., Steele, L., Langenfelds, R.L., Francey, R.J., Barnola, J.M., & Morgan, V. (1996). Natural and  
877 anthropogenic changes in atmospheric CO<sub>2</sub> over the last 1000 years from air in Antarctic ice and firn. *Journal of  
878 Geophysical Research: Atmospheres*, 101, 4115-4128
- 879 Evensen, G. (2004). Sampling strategies and square root analysis schemes for the EnKF. *Ocean dynamics*, 54, 539-560
- 880 Exbrayat, J.F., Bloom, A.A., Carvalhais, N. et al. Understanding the Land Carbon Cycle with Space Data: Current Status  
881 and Prospects. *Surv Geophys* 40, 735–755 (2019). <https://doi.org/10.1007/s10712-019-09506-2>
- 882 Fang, H., Baret, F., Plummer, S., & Schaepman - Strub, G. (2019). An overview of global leaf area index (LAI): Methods,  
883 products, validation, and applications. *Reviews of Geophysics*, 57, 739-799
- 884 Fang, H., Beaudoin, H.K., Rodell, M., Teng, W.L., & Vollmer, B.E. (2009). Global Land data assimilation system  
885 (GLDAS) products, services and application from NASA hydrology data and information services center (HDISC). In,  
886 *ASPRS 2009 Annual Conference, Baltimore, Maryland* (pp. 8-13)



- 887 Fang, H., & Liang, S. (2005). A hybrid inversion method for mapping leaf area index from MODIS data: Experiments  
888 and application to broadleaf and needleleaf canopies. *Remote Sensing of Environment*, *94*, 405-424
- 889 Feng, F., Chen, J., Li, X., Yao, Y., Liang, S., Liu, M., Zhang, N., Guo, Y., Yu, J., & Sun, M. (2015). Validity of five  
890 satellite-based latent heat flux algorithms for semi-arid ecosystems. *Remote Sensing*, *7*, 16733-16755
- 891 Friedl, M.A., Sulla-Menashe, D., Tan, B., Schneider, A., Ramankutty, N., Sibley, A., & Huang, X. (2010). MODIS  
892 Collection 5 global land cover: Algorithm refinements and characterization of new datasets. *Remote Sensing of  
893 Environment*, *114*, 168-182
- 894 Gokmen, M., Vekerdy, Z., Verhoef, A., Verhoef, W., Batelaan, O., & Van der Tol, C. (2012). Integration of soil moisture  
895 in SEBS for improving evapotranspiration estimation under water stress conditions. *Remote Sensing of Environment*,  
896 *121*, 261-274
- 897 Gonsamo, A., & Chen, J.M. (2011). Evaluation of the GLC2000 and NALC2005 land cover products for LAI retrieval  
898 over Canada. *Canadian Journal of Remote Sensing*, *37*, 302-313
- 899 Haxeltine, A., & Prentice, I.C. (1996). BIOME3: An equilibrium terrestrial biosphere model based on ecophysiological  
900 constraints, resource availability, and competition among plant functional types. *Global biogeochemical cycles*, *10*, 693-  
901 709
- 902 Hayes, D.J., Turner, D.P., Stinson, G., McGuire, A.D., Wei, Y., West, T.O., Heath, L.S., De Jong, B., McConkey, B.G.,  
903 & Birdsey, R.A. (2012). Reconciling estimates of the contemporary North American carbon balance among terrestrial  
904 biosphere models, atmospheric inversions, and a new approach for estimating net ecosystem exchange from inventory -  
905 based data. *Global Change Biology*, *18*, 1282-1299
- 906 He, L., Chen, J.M., Liu, J., Bélair, S., & Luo, X. (2017). Assessment of SMAP soil moisture for global simulation of  
907 gross primary production. *Journal of Geophysical Research: Biogeosciences*, *122*, 1549-1563
- 908 Huang, C., Li, Y., Gu, J., Lu, L., & Li, X. (2015). Improving estimation of evapotranspiration under water-limited  
909 conditions based on SEBS and MODIS data in arid regions. *Remote Sensing*, *7*, 16795-16814
- 910 Ines, A.V., Das, N.N., Hansen, J.W., & Njoku, E.G. (2013). Assimilation of remotely sensed soil moisture and vegetation  
911 with a crop simulation model for maize yield prediction. *Remote Sensing of Environment*, *138*, 149-164
- 912 Jacqueline, E., Al Bitar, A., Mialon, A., Kerr, Y., Quesney, A., Cabot, F., & Richaume, P. (2010). SMOS CATDS level  
913 3 global products over land. In, *Remote Sensing for Agriculture, Ecosystems, and Hydrology XII* (p. 78240K):  
914 International Society for Optics and Photonics
- 915 Kaminski, T., Scholze, M., Vossbeck, M., Knorr, W., Buchwitz, M., & Reuter, M. (2017). Constraining a terrestrial  
916 biosphere model with remotely sensed atmospheric carbon dioxide. *Remote Sensing of Environment*, *203*, 109-124
- 917 Kato, T., Knorr, W., Scholze, M., Veenendaal, E., Kaminski, T., Kattge, J., & Gobron, N. (2013). Simultaneous  
918 assimilation of satellite and eddy covariance data for improving terrestrial water and carbon simulations at a semi-arid  
919 woodland site in Botswana. *Biogeosciences*, *10*, 789-802
- 920 Keeling, C.D., Whorf, T.P., Wahlen, M., & Van der Plichtt, J. (1995). Interannual extremes in the rate of rise of  
921 atmospheric carbon dioxide since 1980. *Nature*, *375*, 666-670
- 922 Keller, M., Schimel, D.S., Hargrove, W.W., & Hoffman, F.M. (2008). A continental strategy for the National Ecological  
923 Observatory Network. *Frontiers in Ecology and the Environment*, *6*, 282-284

- 924 Kganyago, M., Mhangara, P., Alexandridis, T., Laneve, G., Ovakoglou, G., & Mashiyyi, N. (2020). Validation of sentinel-  
 925 2 leaf area index (LAI) product derived from SNAP toolbox and its comparison with global LAI products in an African  
 926 semi-arid agricultural landscape. *Remote Sensing Letters*, *11*, 883-892
- 927 Khan, M.S., Liaqat, U.W., Baik, J., & Choi, M. (2018). Stand-alone uncertainty characterization of GLEAM, GLDAS  
 928 and MOD16 evapotranspiration products using an extended triple collocation approach. *Agricultural and Forest  
 929 Meteorology*, *252*, 256-268
- 930 Kim, H., Parinussa, R., Konings, A.G., Wagner, W., Cosh, M.H., Lakshmi, V., Zohaib, M., & Choi, M. (2018). Global-  
 931 scale assessment and combination of SMAP with ASCAT (active) and AMSR2 (passive) soil moisture products. *Remote  
 932 Sensing of Environment*, *204*, 260-275
- 933 Koster, R.D., Crow, W.T., Reichle, R.H., & Mahanama, S.P. (2018). Estimating basin - scale water budgets with SMAP  
 934 soil moisture data. *Water resources research*, *54*, 4228-4244
- 935 Law, B., Falge, E., Gu, L.v., Baldocchi, D., Bakwin, P., Berbigier, P., Davis, K., Dolman, A., Falk, M., & Fuentes, J.  
 936 (2002). Environmental controls over carbon dioxide and water vapor exchange of terrestrial vegetation. *Agricultural and  
 937 Forest Meteorology*, *113*, 97-120
- 938 Lee, H., Seo, D.-J., & Koren, V. (2011). Assimilation of streamflow and in situ soil moisture data into operational  
 939 distributed hydrologic models: Effects of uncertainties in the data and initial model soil moisture states. *Advances in  
 940 water resources*, *34*, 1597-1615
- 941 Li, B., & Rodell, M. (2013). Spatial variability and its scale dependency of observed and modeled soil moisture over  
 942 different climate regions. *Hydrology and Earth System Sciences*, *17*, 1177-1188
- 943 Li C, Tang G, Hong Y. Cross-evaluation of ground-based, multi-satellite and reanalysis precipitation products:  
 944 Applicability of the Triple Collocation method across Mainland China[J]. *Journal of Hydrology*, 2018, 562: 71-83.
- 945 Li, S., Wang, G., Sun, S., Chen, H., Bai, P., Zhou, S., Huang, Y., Wang, J., & Deng, P. (2018). Assessment of multi-  
 946 source evapotranspiration products over china using eddy covariance observations. *Remote Sensing*, *10*, 1692
- 947 Li, S., Zhang, L., Ma, R., Yan, M., & Tian, X. (2020). Improved ET assimilation through incorporating SMAP soil  
 948 moisture observations using a coupled process model: A study of US arid and semiarid regions. *Journal of hydrology*,  
 949 *590*, 125402
- 950 Li, X., Cheng, G., Liu, S., Xiao, Q., Ma, M., Jin, R., Che, T., Liu, Q., Wang, W., & Qi, Y. (2013). Heihe watershed allied  
 951 telemetry experimental research (HiWATER): Scientific objectives and experimental design. *Bulletin of the American  
 952 Meteorological Society*, *94*, 1145-1160
- 953 Li, X., Mao, F., Du, H., Zhou, G., Xu, X., Han, N., Sun, S., Gao, G., & Chen, L. (2017). Assimilating leaf area index of  
 954 three typical types of subtropical forest in China from MODIS time series data based on the integrated ensemble Kalman  
 955 filter and PROSAIL model. *ISPRS Journal of Photogrammetry and Remote Sensing*, *126*, 68-78
- 956 Li, X., & Xiao, J. (2019). A global, 0.05-degree product of solar-induced chlorophyll fluorescence derived from OCO-  
 957 2, MODIS, and reanalysis data. *Remote Sensing*, *11*, 517
- 958 Liang, S., Zhao, X., Liu, S., Yuan, W., Cheng, X., Xiao, Z., Zhang, X., Liu, Q., Cheng, J., & Tang, H. (2013). A long-  
 959 term Global LAnd Surface Satellite (GLASS) data-set for environmental studies. *International Journal of Digital Earth*,  
 960 *6*, 5-33

- 961 Lievens, H., Tomer, S.K., Al Bitar, A., De Lannoy, G.J., Drusch, M., Dumedah, G., Franssen, H.-J.H., Kerr, Y.H.,  
 962 Martens, B., & Pan, M. (2015). SMOS soil moisture assimilation for improved hydrologic simulation in the Murray  
 963 Darling Basin, Australia. *Remote Sensing of Environment*, *168*, 146-162
- 964 Ling, X.-L., Fu, C.-B., Yang, Z.-L., & Guo, W.-D. (2019). Comparison of different sequential assimilation algorithms  
 965 for satellite-derived leaf area index using the Data Assimilation Research Testbed (version Lanai). *Geoscientific Model*  
 966 *Development*, *12*, 3119-3133
- 967 Liu, L., Gudmundsson, L., Hauser, M., Qin, D., Li, S., & Seneviratne, S.I. (2020). Soil moisture dominates dryness stress  
 968 on ecosystem production globally. *Nature communications*, *11*, 1-9
- 969 Liu, Y., Xiao, J., Ju, W., Zhu, G., Wu, X., Fan, W., Li, D., & Zhou, Y. (2018). Satellite-derived LAI products exhibit  
 970 large discrepancies and can lead to substantial uncertainty in simulated carbon and water fluxes. *Remote Sensing of*  
 971 *Environment*, *206*, 174-188
- 972 Ma, H., Huang, J., Zhu, D., Liu, J., Su, W., Zhang, C., & Fan, J. (2013). Estimating regional winter wheat yield by  
 973 assimilation of time series of HJ-1 CCD NDVI into WOFOST-ACRM model with Ensemble Kalman Filter.  
 974 *Mathematical and Computer Modelling*, *58*, 759-770
- 975 Ma, R., Zhang, L., Tian, X., Zhang, J., Yuan, W., Zheng, Y., Zhao, X., & Kato, T. (2017). Assimilation of remotely-  
 976 sensed leaf area index into a dynamic vegetation model for gross primary productivity estimation. *Remote Sensing*, *9*,  
 977 188
- 978 MacBean, N., Peylin, P., Chevallier, F., Scholze, M., & Schürmann, G. (2016). Consistent assimilation of multiple data  
 979 streams in a carbon cycle data assimilation system. *Geoscientific Model Development*, *9*, 3569-3588
- 980 Martens, B., Miralles, D.G., Lievens, H., Schalie, R.v.d., De Jeu, R.A., Fernández-Prieto, D., Beck, H.E., Dorigo, W.A.,  
 981 & Verhoest, N.E. (2017). GLEAM v3: Satellite-based land evaporation and root-zone soil moisture. *Geoscientific Model*  
 982 *Development*, *10*, 1903-1925
- 983 Miernecki, M., Wigneron, J.-P., Lopez-Baeza, E., Kerr, Y., De Jeu, R., De Lannoy, G.J., Jackson, T.J., O'Neill, P.E.,  
 984 Schwank, M., & Moran, R.F. (2014). Comparison of SMOS and SMAP soil moisture retrieval approaches using tower-  
 985 based radiometer data over a vineyard field. *Remote Sensing of Environment*, *154*, 89-101
- 986 Miralles, D.G., Jiménez, C., Jung, M., Michel, D., Ershadi, A., McCabe, M., Hirschi, M., Martens, B., Dolman, A.J., &  
 987 Fisher, J.B. (2016). The WACMOS-ET project-Part 2: Evaluation of global terrestrial evaporation data sets. *Hydrology*  
 988 *and Earth System Sciences*, *20*, 823-842
- 989 Mitchell, H.L., Houtekamer, P.L., & Pellerin, G. (2002). Ensemble size, balance, and model-error representation in an  
 990 ensemble Kalman filter. *Monthly weather review*, *130*, 2791-2808
- 991 Mu, Q., Zhao, M., Heinsch, F.A., Liu, M., Tian, H., & Running, S.W. (2007). Evaluating water stress controls on primary  
 992 production in biogeochemical and remote sensing based models. *Journal of Geophysical Research: Biogeosciences*, *112*
- 993 New, M., Hulme, M., & Jones, P. (2000). Representing twentieth-century space-time climate variability. Part II:  
 994 Development of 1901-96 monthly grids of terrestrial surface climate. *Journal of climate*, *13*, 2217-2238
- 995 Nijssen, B., & Lettenmaier, D.P. (2004). Effect of precipitation sampling error on simulated hydrological fluxes and  
 996 states: Anticipating the Global Precipitation Measurement satellites. *Journal of Geophysical Research: Atmospheres*,  
 997 *109*

- 998 O'Neill, P., Entekhabi, D., Njoku, E., & Kellogg, K. (2010). The NASA soil moisture active passive (SMAP) mission:  
999 Overview. In, *2010 IEEE International Geoscience and Remote Sensing Symposium* (pp. 3236-3239): IEEE
- 1000 O'Carroll, A.G., Eyre, J.R., & Saunders, R.W. (2008). Three-way error analysis between AATSR, AMSR-E, and in situ  
1001 sea surface temperature observations. *Journal of atmospheric and oceanic technology*, 25, 1197-1207
- 1002 Pan, H.; Chen, Z.; de Wit, A.; Ren, J. Joint Assimilation of Leaf Area Index and Soil Moisture from Sentinel-1 and  
1003 Sentinel-2 Data into the WOFOST Model for Winter Wheat Yield Estimation. *Sensors* 2019, 19, 3161.
- 1004 Pardo, N., Sánchez, M.L., Timmermans, J., Su, Z., Pérez, I.A., & García, M.A. (2014). SEBS validation in a Spanish  
1005 rotating crop. *Agricultural and Forest Meteorology*, 195, 132-142
- 1006 Petropoulos, G.P., Ireland, G., & Barrett, B. (2015). Surface soil moisture retrievals from remote sensing: Current status,  
1007 products & future trends. *Physics and Chemistry of the Earth, Parts A/B/C*, 83, 36-56
- 1008 Pipunic, R., Walker, J., & Western, A. (2008). Assimilation of remotely sensed data for improved latent and sensible  
1009 heat flux prediction: A comparative synthetic study. *Remote Sensing of Environment*, 112, 1295-1305
- 1010 Purdy, A.J., Fisher, J.B., Goulden, M.L., Colliander, A., Halverson, G., Tu, K., & Famiglietti, J.S. (2018). SMAP soil  
1011 moisture improves global evapotranspiration. *Remote Sensing of Environment*, 219, 1-14
- 1012 Rahman, A.; Maggioni, V.; Zhang, X.; Houser, P.; Sauer, T.; Mocko, D.M. The Joint Assimilation of Remotely Sensed  
1013 Leaf Area Index and Surface Soil Moisture into a Land Surface Model. *Remote Sens.* 2022, 14, 437.  
1014 <https://doi.org/10.3390/rs14030437>
- 1015 Rüdiger, C., Albergel, C., Mahfouf, J.F., Calvet, J.C., & Walker, J.P. (2010). Evaluation of the observation operator  
1016 Jacobian for leaf area index data assimilation with an extended Kalman filter. *Journal of Geophysical Research:  
1017 Atmospheres*, 115Reichle, R.H., De Lannoy, G.J., Liu, Q., Koster, R.D., Kimball, J.S., Crow, W.T., Ardizzone, J.V.,  
1018 Chakraborty, P., Collins, D.W., & Conaty, A.L. (2017). Global assessment of the SMAP level-4 surface and root-zone  
1019 soil moisture product using assimilation diagnostics. *Journal of Hydrometeorology*, 18, 3217-3237
- 1020 Reichle, R.H., & Koster, R.D. (2004). Bias reduction in short records of satellite soil moisture. *Geophysical Research  
1021 Letters*, 31
- 1022 Rienecker, M.M., Suarez, M.J., Gelaro, R., Todling, R., Bacmeister, J., Liu, E., Bosilovich, M.G., Schubert, S.D., Takacs,  
1023 L., & Kim, G.-K. (2011). MERRA: NASA's modern-era retrospective analysis for research and applications. *Journal of  
1024 climate*, 24, 3624-3648
- 1025 Running, S.W., Nemani, R.R., Heinsch, F.A., Zhao, M., Reeves, M., & Hashimoto, H. (2004). A continuous satellite-  
1026 derived measure of global terrestrial primary production. *Bioscience*, 54, 547-560
- 1027 Scholze, M., Buchwitz, M., Dorigo, W., Guanter, L., and Quegan, S.: Reviews and syntheses: Systematic Earth  
1028 observations for use in terrestrial carbon cycle data assimilation systems, *Biogeosciences*, 14, 3401–3429,  
1029 <https://doi.org/10.5194/bg-14-3401-2017>, 2017.
- 1030 Seneviratne, S.I., Corti, T., Davin, E.L., Hirschi, M., Jaeger, E.B., Lehner, I., Orlowsky, B., & Teuling, A.J. (2010).  
1031 Investigating soil moisture–climate interactions in a changing climate: A review. *Earth-Science Reviews*, 99, 125-161
- 1032 Sitch, S., Smith, B., Prentice, I.C., Arneth, A., Bondeau, A., Cramer, W., Kaplan, J.O., Levis, S., Lucht, W., & Sykes,  
1033 M.T. (2003). Evaluation of ecosystem dynamics, plant geography and terrestrial carbon cycling in the LPJ dynamic  
1034 global vegetation model. *Global Change Biology*, 9, 161-185

- 1035 Stoffelen, A. (1998). Toward the true near - surface wind speed: Error modeling and calibration using triple collocation.  
1036 *Journal of geophysical research: oceans*, 103, 7755-7766
- 1037 Sun, P., Wu, Y., Xiao, J., Hui, J., Hu, J., Zhao, F., Qiu, L., & Liu, S. (2019). Remote sensing and modeling fusion for  
1038 investigating the ecosystem water-carbon coupling processes. *Science of the total environment*, 697, 134064
- 1039 Taylor, K.E. (2001). Summarizing multiple aspects of model performance in a single diagram. *Journal of Geophysical*  
1040 *Research: Atmospheres*, 106, 7183-7192
- 1041 Tian, S., Renzullo, L.J., Van Dijk, A.I., Tregoning, P., & Walker, J.P. (2019). Global joint assimilation of GRACE and  
1042 SMOS for improved estimation of root-zone soil moisture and vegetation response. *Hydrology and Earth System*  
1043 *Sciences*, 23, 1067-1081
- 1044 Tian, X., & Feng, X. (2015). A non-linear least squares enhanced POD-4DVar algorithm for data assimilation. *Tellus A:*  
1045 *Dynamic Meteorology and Oceanography*, 67, 25340
- 1046 Tian, X., Xie, Z., Dai, A., Jia, B., & Shi, C. (2010). A microwave land data assimilation system: Scheme and preliminary  
1047 evaluation over China. *Journal of Geophysical Research: Atmospheres*, 115
- 1048 Tian, X., Xie, Z., Dai, A., Shi, C., Jia, B., Chen, F., & Yang, K. (2009). A dual - pass variational data assimilation  
1049 framework for estimating soil moisture profiles from AMSR - E microwave brightness temperature. *Journal of*  
1050 *Geophysical Research: Atmospheres*, 114
- 1051 Tian, X., Xie, Z., Liu, Y., Cai, Z., Fu, Y., Zhang, H., & Feng, L. (2014). A joint data assimilation system (Tan-Tracker)  
1052 to simultaneously estimate surface CO<sub>2</sub> fluxes and 3-D atmospheric CO<sub>2</sub> concentrations from observations.  
1053 *Atmospheric Chemistry and Physics*, 14, 13281-13293
- 1054 Tian, X., Xie, Z., & Sun, Q. (2011). A POD-based ensemble four-dimensional variational assimilation method. *Tellus*  
1055 *A: Dynamic Meteorology and Oceanography*, 63, 805-816
- 1056 Trugman, A., Medvigy, D., Mankin, J., & Anderegg, W. (2018). Soil moisture stress as a major driver of carbon cycle  
1057 uncertainty. *Geophysical Research Letters*, 45, 6495-6503
- 1058 Turner, D.P., Ritts, W.D., Cohen, W.B., Gower, S.T., Running, S.W., Zhao, M., Costa, M.H., Kirschbaum, A.A., Ham,  
1059 J.M., & Saleska, S.R. (2006). Evaluation of MODIS NPP and GPP products across multiple biomes. *Remote Sensing of*  
1060 *Environment*, 102, 282-292
- 1061 Turner, D.P., Ritts, W.D., Cohen, W.B., Maeirsperger, T.K., Gower, S.T., Kirschbaum, A.A., Running, S.W., Zhao, M.,  
1062 Wofsy, S.C., & Dunn, A.L. (2005). Site - level evaluation of satellite - based global terrestrial gross primary production  
1063 and net primary production monitoring. *Global Change Biology*, 11, 666-684
- 1064 Twine, T.E., Kustas, W., Norman, J., Cook, D., Houser, P., Meyers, T., Prueger, J., Starks, P., & Wesely, M. (2000).  
1065 Correcting eddy-covariance flux underestimates over a grassland. *Agricultural and Forest Meteorology*, 103, 279-300
- 1066 Wang, L., Zhu, H., Lin, A., Zou, L., Qin, W., & Du, Q. (2017). Evaluation of the latest MODIS GPP products across  
1067 multiple biomes using global eddy covariance flux data. *Remote Sensing*, 9, 418
- 1068 Waring, R.H., & Running, S.W. (2010). *Forest ecosystems: analysis at multiple scales*. Elsevier
- 1069 Wieder, W., Boehnert, J., Bonan, G., & Langseth, M. (2014). RegridDED harmonized world soil database v1. 2. *ORNL*  
1070 *DAAC*

- 1071 Wu, M.; Scholze, M.; Voßbeck, M.; Kaminski, T.; Hoffmann, G. Simultaneous Assimilation of Remotely Sensed Soil  
1072 Moisture and FAPAR for Improving Terrestrial Carbon Fluxes at Multiple Sites Using CCDAS. *Remote Sens.* 2019, 11,  
1073 27. <https://doi.org/10.3390/rs11010027>
- 1074 Xiao, J., Chevallier, F., Gomez, C., Guanter, L., Hicke, J.A., Huete, A.R., Ichii, K., Ni, W., Pang, Y., & Rahman, A.F.  
1075 (2019). Remote sensing of the terrestrial carbon cycle: A review of advances over 50 years. *Remote Sensing of*  
1076 *Environment*, 233, 111383
- 1077 Xiao, Z., Liang, S., & Jiang, B. (2017). Evaluation of four long time-series global leaf area index products. *Agricultural*  
1078 *and Forest Meteorology*, 246, 218-230
- 1079 Xiao, Z., Liang, S., Wang, J., Chen, P., Yin, X., Zhang, L., & Song, J. (2013). Use of general regression neural networks  
1080 for generating the GLASS leaf area index product from time-series MODIS surface reflectance. *IEEE Transactions on*  
1081 *Geoscience and Remote Sensing*, 52, 209-223
- 1082 Xiao, Z., Liang, S., Wang, J., Xiang, Y., Zhao, X., & Song, J. (2016). Long-time-series global land surface satellite leaf  
1083 area index product derived from MODIS and AVHRR surface reflectance. *IEEE Transactions on Geoscience and*  
1084 *Remote Sensing*, 54, 5301-5318
- 1085 Xie, Y.; Wang, P.; Sun, H.; Zhang, S.; Li, L. Assimilation of Leaf Area Index and Surface Soil Moisture With the  
1086 CERES-Wheat Model for Winter Wheat Yield Estimation Using a Particle Filter Algorithm. *IEEE J. Sel. Top. Appl.*  
1087 *Earth Obs. Remote Sens.* 2017, 10, 1303–1316.
- 1088 Yan, M., Tian, X., Li, Z., Chen, E., Wang, X., Han, Z., & Sun, H. (2016). Simulation of forest carbon fluxes using model  
1089 incorporation and data assimilation. *Remote Sensing*, 8, 567
- 1090 Yang, W., Wang, Y., Liu, X., Zhao, H., Shao, R., & Wang, G. (2020). Evaluation of the rescaled complementary  
1091 principle in the estimation of evaporation on the Tibetan Plateau. *Science of the total environment*, 699, 134367
- 1092 Yang, X., Yong, B., Ren, L., Zhang, Y., & Long, D. (2017). Multi-scale validation of GLEAM evapotranspiration  
1093 products over China via ChinaFLUX ET measurements. *International Journal of Remote Sensing*, 38, 5688-5709
- 1094 Yilmaz, M.T., & Crow, W.T. (2014). Evaluation of assumptions in soil moisture triple collocation analysis. *Journal of*  
1095 *Hydrometeorology*, 15, 1293-1302
- 1096 Yuan, W., Liu, S., Yu, G., Bonnefond, J.-M., Chen, J., Davis, K., Desai, A.R., Goldstein, A.H., Gianelle, D., & Rossi,  
1097 F. (2010). Global estimates of evapotranspiration and gross primary production based on MODIS and global  
1098 meteorology data. *Remote Sensing of Environment*, 114, 1416-1431
- 1099 Zhang, D.-H., Li, X.-R., Zhang, F., Zhang, Z.-S., & Chen, Y.-L. (2016). Effects of rainfall intensity and intermittency  
1100 on woody vegetation cover and deep soil moisture in dryland ecosystems. *Journal of hydrology*, 543, 270-282
- 1101 Zhang, F., & Weng, Y. (2015). Predicting hurricane intensity and associated hazards: A five-year real-time forecast  
1102 experiment with assimilation of airborne Doppler radar observations. *Bulletin of the American Meteorological Society*,  
1103 96, 25-33
- 1104 Zhang, L., Xiao, J., Zheng, Y., Li, S., & Zhou, Y. (2020). Increased carbon uptake and water use efficiency in global  
1105 semi-arid ecosystems. *Environmental Research Letters*, 15, 034022
- 1106 Zhang, X., Huang, X.-Y., Liu, J., Poterjoy, J., Weng, Y., Zhang, F., & Wang, H. (2014). Development of an efficient  
1107 regional four-dimensional variational data assimilation system for WRF. *Journal of atmospheric and oceanic technology*,  
1108 31, 2777-2794

- 1109 Zhang, R., Kim, S., & Sharma, A. (2019). A comprehensive validation of the SMAP Enhanced Level-3 Soil Moisture  
1110 product using ground measurements over varied climates and landscapes. *Remote Sensing of Environment*, 223, 82-94
- 1111 Zhao, L., Xia, J., Xu, C.-y., Wang, Z., Sobkowiak, L., & Long, C. (2013). Evapotranspiration estimation methods in  
1112 hydrological models. *Journal of Geographical Sciences*, 23, 359-369
- 1113 Zobitz, J., Moore, D.J., Quaife, T., Braswell, B.H., Bergeson, A., Anthony, J.A., & Monson, R.K. (2014). Joint data  
1114 assimilation of satellite reflectance and net ecosystem exchange data constrains ecosystem carbon fluxes at a high-  
1115 elevation subalpine forest. *Agricultural and Forest Meteorology*, 195, 73-88
- 1116 Zou, L., Zhan, C., Xia, J., Wang, T., & Gippel, C.J. (2017). Implementation of evapotranspiration data assimilation with  
1117 catchment scale distributed hydrological model via an ensemble Kalman filter. *Journal of hydrology*, 549, 685-702
- 1118